

DIGIT survey of far-infrared lines from protoplanetary disks II. [O I], [C II], OH, H₂O and CH⁺.

D. Fedele¹, S. Bruderer¹, E.F. van Dishoeck^{1,2}, N.J. Evans II³, G. Meeus⁴, J. Bouwman⁵, J. Carr⁶, Th. Henning⁵, G.J. Herczeg⁷, J. Green³, J.R. Najita⁸, C. Salyk⁹

¹ Max Planck Institut für Extraterrestrische Physik, Giessenbachstrasse 1, 85748 Garching, Germany

² Leiden Observatory, Leiden University, P.O. Box 9513, 2300 RA Leiden, The Netherlands

³ University of Texas at Austin, Department of Astronomy, 2515 Speedway, Stop C1400, Austin TX 78712-1205, USA

⁴ Universidad Autonoma de Madrid, Dpt. Fisica Teorica, Campus Cantoblanco, Spain

⁵ Max Planck Institute for Astronomy, Königstuhl 17, 69117, Heidelberg, Germany

⁶ Naval Research Laboratory, Code 7211, Washington, DC 20375, USA

⁷ Kavli Institute for Astronomy and Astrophysics, Yi He Yuan Lu 5, Beijing, 100871, P.R. China

⁸ National Optical Astronomy Observatory, 950 N. Cherry Avenue, Tucson, AZ 85719, USA

⁹ McDonald Observatory, The University of Texas at Austin, 1 University Station, C1402, Austin, TX 78712, USA

Preprint online version: November 27, 2012

ABSTRACT

We present far-infrared (50–200 μm) spectroscopic observations of young pre-main-sequence (PMS) stars. The observations were taken with *Herschel*/PACS as part of the DIGIT key project. The sample includes 16 Herbig AeBe and 4 T Tauri sources observed in SED mode covering the entire spectral range. An additional 6 Herbig AeBe and 4 T Tauri systems have been observed in SED mode with a limited spectral coverage. Multiple atomic fine structure and molecular lines are detected: [O I], [C II], CO, OH, H₂O, CH⁺, with the CO results reported in Meeus et al. (2013). The most common feature is the [O I] 63 μm line detected in almost all of the sources followed by OH. In contrast with CO, OH is detected toward both Herbig AeBe groups (flared and non-flared sources). This difference is likely due to different excitation mechanisms, with CO requiring UV radiation to heat the gas and excite the molecule while OH can also be effectively pumped by infrared radiation. A LTE slab model fit to the OH lines indicates column densities $10^{13} < N_{\text{OH}} < 10^{17} \text{cm}^{-2}$, emitting radius $20 < r < 50 \text{ AU}$ and excitation temperature $200 < T_{\text{ex}} < 500 \text{ K}$. The OH emission comes from an intermediate layer in the disk at stellar distances of order 30 AU. Two sources (HD 50138 and DG Tau) show a lower excitation temperature ($T_{\text{ex}} \sim 100 \text{ K}$) and larger emitting radius ($50 < R < 100 \text{ AU}$). In this case a further contribution to the OH emission likely comes from an outflow. Warm H₂O emission is detected through multiple lines toward T Tauri systems but only through line stacking in three Herbig AeBe sources (HD 104237, HD 142527, HD 163296). This finding suggests that warm H₂O is present in the outer disk of at least some intermediate-mass pre-main sequence stars, in contrast to the inner disk which is H₂O-poor due to rapid photodissociation. However a non-disk origin (e.g. outflow) cannot be ruled out. The analysis of the oxygen fine structure lines suggests a systematic temperature difference between HAeBe group I and II with the first having a higher gas temperature in the outer disk. This is in agreement with the hypothesis that the two groups of disks have different scale heights in the outer disk. Within group I sources the intensity of the [O I] 63 μm line varies by more than 2 orders of magnitude. This implies a different density and temperature distribution of the outer disk ($> 50 \text{ AU}$). The [C II] emission is spatially extended in all the sources where the line is detected. This is in contrast to the oxygen emission which is co-spatial with the continuum emission. This suggests that not all the [C II] emission is associated with the disk and that there is a contribution from diffuse material around the young stars. The [O I] 145 μm and [C II] lines are only detected toward the [O I] 63 μm -bright sources.

Key words. Protoplanetary disks – Stars: formation

1. Introduction

Far-infrared spectroscopic observations of young pre-main-sequence stars have the potential to reveal the gas and dust composition of protoplanetary disks in regions not probed at any other wavelengths (e.g., van Dishoeck 2004; Lorenzetti 2005; Henning et al. 2010). The atomic and molecular transitions in the far-infrared regime (50–200 μm) span a large range in upper energy level (from a few 10 K to a few 10³ K) and are sensitive to the warm (a few 10² K) upper layers of the disk ($n < 10^8 \text{cm}^{-3}$). For a passively heated disk by UV and/or X-rays from the pre-main-sequence star, these conditions are found at intermediate distances from the central star ($r \gtrsim 10 \text{ AU}$) (e.g., Kamp &

Dullemond 2004; Bruderer et al. 2012). Observations of lines of multiple species provide a wealth of information that allow us to (1) determine the physical properties of the gas such as excitation temperature, column density, emitting radii (and in some cases the total gas density); (2) constrain the excitation mechanism (e.g., collisions, UV fluorescence, IR pumping); and (3) address the chemical structure of the disk. The far-infrared (IR) spectrum contains information complementary to that provided by near- and mid-IR observations which are sensitive to the hot ($> 1000 \text{ K}$) inner region of the disk ($< \text{few AU}$). At the other end of the spectrum, (sub)millimeter spectroscopic observations with ALMA will unveil the physical conditions and chemical composition of the disk midplane at distances $r \gtrsim 10 \text{ AU}$. The far-infrared data probe the intermediate disk radii. The ultimate goal of these observational campaigns is to use the combined

Send offprint requests to: Davide Fedele,
e-mail: fedele@mppe.mpg.de

data to address the chemistry and physics of the entire protoplanetary disk from inner to outer edge.

We present here 50–200 μm spectra of a sample of protoplanetary disks around Herbig AeBe and T Tauri stars obtained in the context of the ‘Dust, Ice and Gas in Time’ (DIGIT) key program (Sturm et al. 2010). The unprecedented sensitivity of the PACS instrument (Poglitsch et al. 2010) on board of the *Herschel* Space Observatory (Pilbratt et al. 2010) allows for the first time to detect weak atomic and molecular emission down to a few $10^{-18} \text{ W m}^{-2}$. Far-IR spectra of bright Herbig stars have been obtained previously with the Long Wavelength Spectrometer (LWS) on the Infrared Space Observatory (ISO) (e.g., Waelkens et al. 1996; Meeus et al. 2001; Lorenzetti et al. 2000, 2002; Creech-Eakman et al. 2002). One of the main results has been an empirical classification of the Herbig AeBe systems into two groups based on the ratio of the far- to near-IR (dust) emission (Meeus et al. 2001). Group I sources have a high far- to near-IR emission ratio consistent with a flaring disk geometry while Group II sources have a low flux ratio characteristic of a flat, self-shadowed disk. Grain growth and settling may also play a role (e.g. Acke et al. 2009). One question to be addressed here is to what extent the far-IR gas-phase lines reflect this dichotomy in disk structure.

The near-IR spectra of Herbig AeBe sources are characterised by several ro-vibrational lines of CO (e.g. Brittain et al. 2003; Blake & Boogert 2004; van der Plas et al. 2009; Salyk et al. 2011a) and OH (Mandell et al. 2008; Fedele et al. 2011). At mid-IR wavelengths the spectrum of an Herbig AeBe star is dominated by dust emission and only a very few Herbig sources show molecular emission (Pontoppidan et al. 2011; Salyk et al. 2011b). In contrast, the emission from T Tauri systems is characterised by a rich molecular spectrum from near- to mid-IR wavelengths. The inventory of molecular species detected in T Tauri sources in the infrared includes: CO (e.g. Najita et al. 2003), OH and H₂O (Salyk et al. 2008, e.g.), HCN and C₂H₂ (e.g. Pascucci et al. 2009; Mandell et al. 2012), CO₂ (Pontoppidan et al. 2011). Are Herbig sources also different from T Tauri sources at far-IR wavelengths?

In this paper we report on the detection of far-IR atomic fine structure lines ([O I] and [C II]) and molecular lines (OH, H₂O, CH⁺). The analysis of far-infrared CO lines is reported in Meeus et al. (in preparation, hereafter paper I). Data for individual T Tauri sources are presented and analyzed in Salyk et al. (in prep., AS 205), Vicente et al. (in prep., S CrA) and Carr et al. (in prep., DG Tau).

2. Observations and data reduction

2.1. Observational details

PACS is an array of 5×5 spaxels¹, with each spaxel covering 9'4×9'4. The instrument is diffraction limited only at $\lambda < 110 \mu\text{m}$. The targets were observed in SED mode with two settings in order to cover the spectral range 51–220 μm (B2A, 51–73 μm , short R1, 100–145 μm and B2B, 70–105 μm long R1, 140–220 μm). The spectral resolving power is $R = \lambda/\Delta\lambda \sim 1000$, increasing to 3000 at the shortest wavelengths. A second sample of targets was observed with a limited spectral range (B2A, 60–75 μm ; short R1, 120–143 μm) centered at the position of the forsterite emission but including some specific lines. The observations were carried out in chopping/nodding mode with a

¹ A spaxel is a spatial sampling element of the PACS integral field unit

chopping throw of 6'. The observation log and parameters of the sample are presented in paper I (Meeus et al. in preparation).

The data have been reduced with HIPE 8.0.2489 with standard calibration files from level 0 to level 2 (see Green et al. in preparation). The two nod positions were reduced separately (oversampling factor = 3, up-sampling factor = 1) and averaged after a flat-field correction. In the case of HD 100546, which was observed in a different mode during the science demonstration phase, we used an oversampling factor equal to 1. The spectra are extracted from the central spaxel to optimize the signal-to-noise (S/N) ratio. To flux calibrate the spectra we performed the following steps: 1) correct for flux loss by means of a PSF-loss correction function provided by HIPE; 2) scale to PACS photometry (whenever available); 3) matching spectral modules. Step 1 is valid for objects well centered in the central spaxel. In the case of mispointed observations we extracted the total flux (all 25 spaxels) to recover the flux loss. In this case we fitted a 3rd-order polynomial to two spectra (central spaxel and 25 spaxels). The correction factor is the ratio between the two fits. The mispointed sources are: AB Aur, HD 97048, HD 169142, HD 142666. The regions affected by spectral leakage (B2B 95 – 105 μm and R1 190 – 220 μm) are excluded from this procedure. Based on a statistical analysis, the PACS SED fluxes agree with PACS photometry to within 5–10%. For this reason we assign an uncertainty of 10% to the PACS SED fluxes of sources without PACS photometry available.

The line fluxes are measured by fitting a Gaussian function and the uncertainty (σ) is given by the product $STD_F \delta\lambda \sqrt{N_{\text{bin}}}$, where STD_F is the standard deviation of the (local) spectrum ($\text{W m}^{-2} \mu\text{m}^{-1}$), $\delta\lambda$ is the wavelength spacing of the bins (μm) and N_{bin} is the width of the line in spectral bins (5).

2.2. Sample

The sources were selected primarily on their far-IR fluxes such that a $S/N \approx 100$ could be reached on the continuum within 5 hours of integration time. The Herbig AeBe sources are all isolated pre-main sequence stars of spectral type F4 to B9 that are not embedded in large molecular clouds. They have been studied previously at mid-IR wavelengths by *Spitzer* (Juhász et al. 2010). The T Tauri stars consist of an inhomogeneous sample of bright sources with K-G spectral type. In total 22 Herbig stars and 8 T Tauri stars have been observed. The focus in this paper is on the Herbig sample, but the data on T Tauri sources are reported for completeness and to allow a comparison with the Herbig sample in a consistent way.

3. Results

3.1. Overview

An overview of the detected atomic and molecular species is shown in Table 1. Fig. 1 shows the continuum normalized PACS spectrum of a T Tauri star (AS 205, TBC) and of an Herbig AeBe star (HD 97048). The strongest and most common feature is the [O I] 63 μm line, seen in all but 4 sources. The [O I] 145 μm and [C II] 157 μm lines are also detected, usually in the same sources, although the detection rate is much lower for these two lines. Four molecular species are seen: CO, OH, H₂O and CH⁺. The fluxes of the detected species are reported in Tables 2 and 3. The CO lines are presented in a paper I. After [O I] 63 μm , OH emission is the most common feature detected, in 40% of the sources with full spectral coverage.

Table 1. Overview of detected species.

ID	Star	[O I] 63 μ m	[O I] 145 μ m	[C II]	CO ^a	OH	H ₂ O	CH ⁺	HD	OH ⁺
1	AB Aur	Y	Y	Y	Y	Y	N	N	N	N
2	HD 36112	Y	N	N	Y	Y	N	N	N	N
3	HD 38120	Y	Y	Y	N	?	N	N	N	N
4	HD 50138	Y	Y	Y	N	Y	N	N	N	N
5	HD 97048	Y	Y	Y	Y	Y	N	Y	N	N
6	HD 100453	Y	N	N	N	N	N	N	N	N
7	HD 100546	Y	Y	Y	Y	Y	N	Y	N	N
8	HD 104237	Y	N	N	N	Y	Y	N	N	N
9	HD 135344 B	Y	N	N	N	N	N	N	N	N
10	HD 139614	Y	N	N	N	N	N	N	N	N
11	HD 142527	Y	N	N	N	?	Y	N	N	N
12	HD 144668	Y	N	N	N	N	N	N	N	N
13	Oph IRS 48	Y	Y	Y	Y	N	N	N	N	N
14	HD 163296	Y	N	N	N	Y	Y	N	N	N
15	HD 169142	Y	N	N	N	N	N	N	N	N
16	HD 179218	Y	Y	Y	N	N	N	N	N	N
17	HD 35187	Y	N ^b	N ^b	N	N	N	N	N	N
18	HD 98922	Y	-	-	N	N	N	N	N	N
19	HD 141569 A	Y	Y ^b	Y ^b	N	N	N	N	N	N
20	HD 142666	N ^c	N ^b	N ^b	N	?	N	N	N	N
21	HD 144432	N	-	-	N	N	N	N	N	N
22	HD 150193	Y	N ^b	N ^b	N	N	N	N	N	N
23	DG Tau	Y	Y	Y	Y	Y	Y	N	N	N
24	AS 205	Y	Y	N	Y	Y	Y	N	N	N
25	EM* SR 21	N	N	Y	N	N	N	N	N	N
26	S CrA	Y	Y	N	Y	Y	Y	N	N	N
27	HT Lup	Y	-	-	N	N	N	N	N	N
28	RU Lup	Y	-	-	N	Y	N	N	N	N
29	RY Lup	Y	-	-	N	N	N	N	N	N
30	RNO 90	Y	-	-	N	Y	Y	N	N	N

Notes. ^(a) The analysis of the CO lines is presented in Paper I. The symbol “-” means species not observed.

^(b) Data not available in DIGIT. Line observed by Meeus et al. (2012).

^(c) Line detected by Meeus et al. (2012).

We searched for other species such as HD and OH⁺. The HD $J=1-0$ line at 112 μ m has been detected towards TW Hya with a flux of $6.3 (\pm 0.7) 10^{-18} \text{ W m}^{-2}$ after deep integration (Bergin et al. in press). None of the sources analyzed here shows evidence of HD or OH⁺ emission with 3σ upper limits of the order of $1-2 10^{-17} \text{ W m}^{-2}$ for most of the sources. Typical upper limits in different parts of the PACS spectrum can be derived from upper limits on nearby OH lines in Table 3.

3.2. [O I]

The [O I] 63 μ m line is the most common and strongest feature detected throughout the whole sample. The only sources for which the line is not detected are HD 142666, HD 144432 and SR 21. The [O I] 63 μ m emission is not spatially extended. The line flux ranges from $10^{-17} - 10^{-15} \text{ W m}^{-2}$. The [O I] 145 μ m line is detected in 7 (out of 16) HAeBe stars and in 3 (out of 4) TT stars, in the central spaxel only. The line flux ranges from $10^{-17} - 10^{-15} \text{ W m}^{-2}$. Fig. 2 shows the [O I] spectra for a selected sample.

3.3. OH

The most common molecular species detected in the PACS spectra is the hydroxyl radical, OH. Six OH doublets with upper energy levels up to 875 K are found including a cross-ladder transition ${}^2\Pi_{1/2} - {}^2\Pi_{3/2} J = 1/2 - 3/2$ at 79 μ m. No spatially extended

OH emission is detected outside the central spaxel of the PACS array. The emission is seen in both Herbig AeBe groups (flared and flat) as well as in T Tauri stars. Fig. 3 shows three OH lines for the nine sources in which at least one doublet is detected.

3.4. H₂O

Far-infrared H₂O lines are readily detected toward T Tauri sources: AS 205, DG Tau, S CrA, and RNO 90 show several lines (Salyk et al., Vicente et al., Carr et al., in prep.). In contrast, Herbig sources show weak or no H₂O far-IR emission. Weak lines have been reported toward HD 163296 (Fedele et al. 2012; Meeus et al. 2012) and have been confirmed through a stacking analysis. Only two other Herbig AeBe stars show hints of H₂O lines: HD 142527 and HD 104237. The lines are weak, with line fluxes ranging between a few $10^{-18} \text{ W m}^{-2}$ to a few $10^{-17} \text{ W m}^{-2}$, often below the 3σ limit. To confirm the presence of H₂O emission in these sources, we performed a line stacking analysis as described in detail in Fedele et al. (2012). In brief, the stacking consists in averaging the spectral segments containing a H₂O line, based on a template of observed H₂O lines by Herczeg et al. (2012). Spectral bins containing other emission lines ([O I], OH, CO and CH⁺) are masked and blended H₂O lines are excluded from the analysis. The stacked H₂O spectra of HD 163296, HD 142527 and HD 104237 are shown in Fig. 4. The false alarm probability, i.e. the probability to detect a signal of equal intensity by stacking random portions of the PACS spectrum, is 0.02 % for HD 142527 and 0.2 % for HD 104237 based

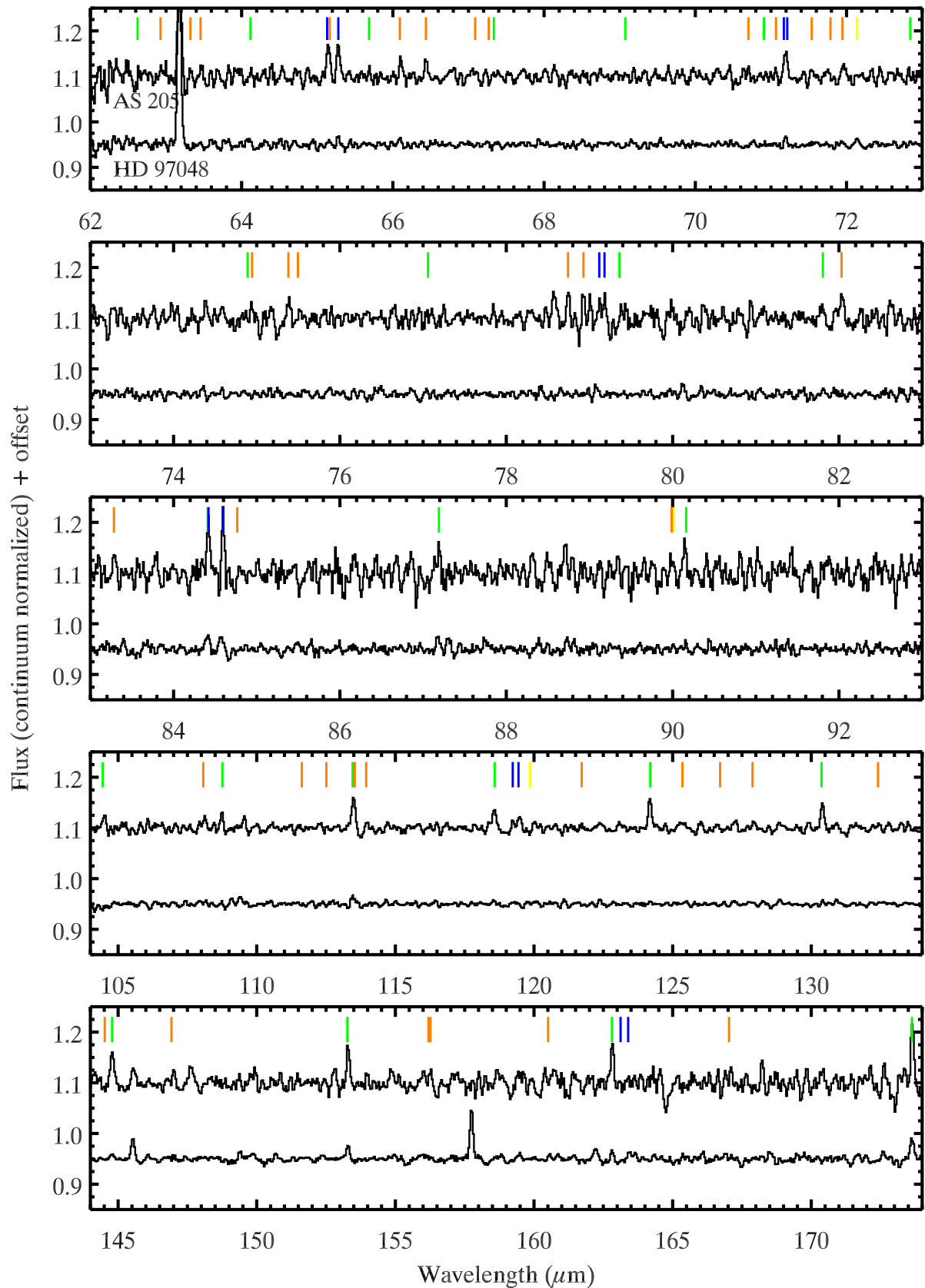


Fig. 1. PACS spectrum (continuum normalized) of AS 205 (top) and HD 97048 (bottom). The marks indicate the position of CO (green), OH (blue), H₂O (orange) and CH⁺ (yellow). The atomic fine structure lines ([O I] 63 μm, [O I] 145 μm and [C II] 157 μm) are easily identified. *TBC: if Colette's paper shows the full AS 205 spectrum, a different sources would be used here*

on 50,000 randomized tests compared to a false alarm probability of < 0.03 % for HD 163296. None of the other Herbig AeBe sources show evidence for the presence of warm H₂O.

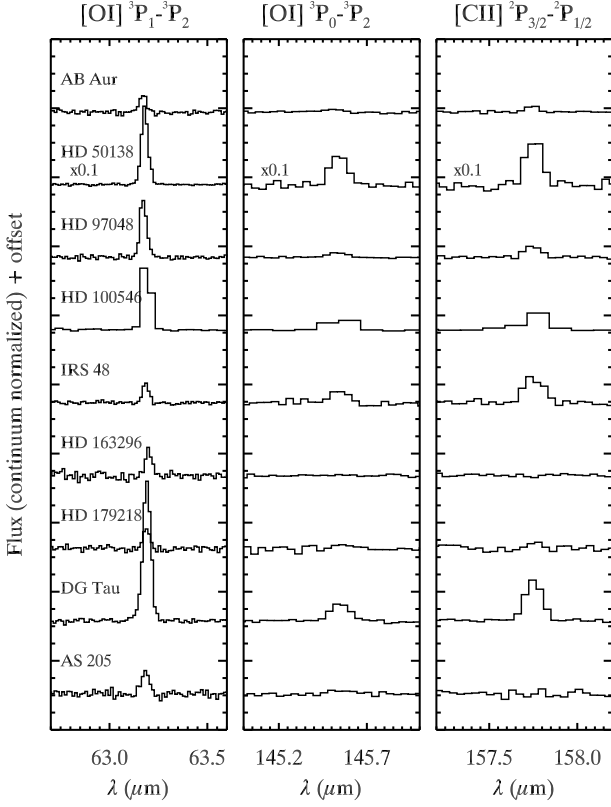


Fig. 2. PACS spectra (central spaxel only) of atomic fine structure lines toward selected sources.

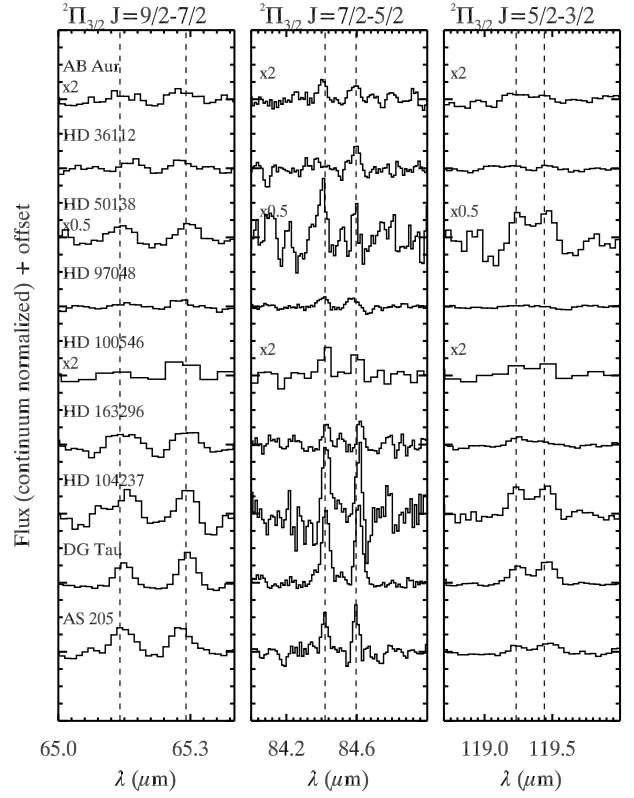


Fig. 3. PACS spectra of various OH doublets.

3.5. CH⁺

The only two sources showing CH⁺ emission are the Herbig Ae systems HD 100546 and HD 97048, Table 4). In the first case six rotational lines are detected (Thi et al. 2011) while in the case of HD 97048 only the $J = 6-5$ ($60.25 \mu\text{m}$) and $J = 5-4$ ($72.14 \mu\text{m}$) lines are seen. The line fluxes in HD 100546 are slightly different from Thi et al. (2011), this is likely due to different flux calibration (see sec.2.1).

3.6. [C II]

[C II] emission is detected towards 7 (out of 16) Herbig AeBe sources and 2 (out of 4) T Tauri stars (Table 2). In contrast with [O I], the [C II] emission is often spatially extended. This suggests that some of the emission is produced in the large scale environment (cloud or remnant envelope) around the star even though very extended emission on $\geq 6'$ scales has been chopped out. More details are given in the Appendix where the [C II] spectral maps are also presented. The [C II] flux reported in Table 2 refers to the on-source spectrum only (see sec. 2.1). These values must be considered as upper limit to the [C II] emission arising from the disk as extended emission from a compact remnant envelope may still be present in the central $9'.4 \times 9'.4$ area of the sky. The closest target is at ~ 100 pc and the size of the central spaxel correspond to a physical scale of ~ 1000 AU squared which is of the same order of a compact envelope. Moreover, given the large PSF at this wavelength, some of the spatially extended emission will fall into the central spaxel.

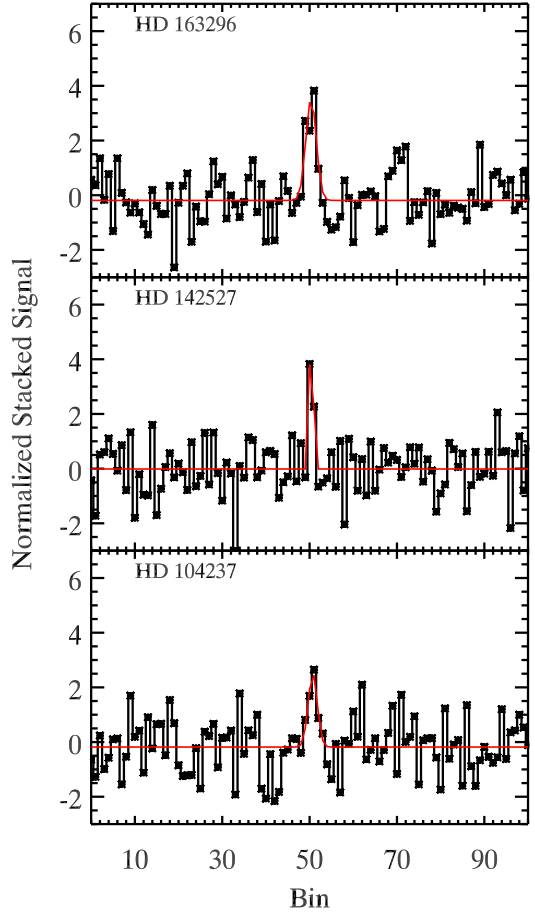


Fig. 4. H₂O line stacking for HD 163296, HD 142527 and HD 104237.

Table 2. [O I] and [C II] line fluxes (10^{-17} W m⁻²)

	[O I] 63 μ m	[O I] 145 μ m	[C II] ^a
AB Aur	94.6 \pm 5.2	3.7 \pm 0.7	2.0
HD 36112	5.6 \pm 0.7	< 1.1	< 1.2
HD 38120	7.6 \pm 0.8	0.7 \pm 0.1	3.3
HD 50138	240 \pm 10	6.6 \pm 0.2	7.8
HD 97048	136 \pm 5	5.3 \pm 0.5	6.3
HD 100453	10.2 \pm 0.7	< 1.2	< 1.3
HD 100546	596 \pm 6	21.1 \pm 1.1	17.6
HD 104237	7.4 \pm 0.7	< 1.5	< 1.5
HD 135344 B	3.6 \pm 0.5	< 1.2	< 1.4
HD 139614	3.1 \pm 0.4	< 1.2	< 1.3
HD 142527	3.6 \pm 0.8	< 2.9	< 2.8
HD 144668	13.3 \pm 1.0	< 0.9	< 1.1
IRS 48	30.8 \pm 1.5	2.9 \pm 0.6	1.2
HD 163296	18.2 \pm 0.9	< 1.3	< 1.3
HD 169142	8.9 \pm 2.0	< 2.2	< 2.5
HD 179218	17.9 \pm 0.9	0.95 \pm 0.1	0.4 ^b
HD 35187	4.8 \pm 2.0	–	–
HD 98922	23.1 \pm 1.2	–	–
HD 141569 A	25.3 \pm 1.5	–	–
HD 142666	< 50	–	–
HD 144432	< 5.6	–	–
HD 150193	3.2 \pm 0.7	–	–
DG Tau	153 \pm 2.0	8.3 \pm 0.4	7.4
AS 205 N	21.5 \pm 1.4	1.6 \pm 0.4	< 1.5
SR 21	< 5.4	< 1.3	0.13
S Cra	43.6 \pm 1.3	1.8 \pm 0.5	< 1.7
HT Lup	4.0 \pm 0.8	–	–
RU Lup	18.9 \pm 1.2	–	–
RY Lup	5.0 \pm 2.0	–	–
RNO 90	12.5 \pm 1.0	–	–

Notes. ^(a) After subtraction of the extended emission.

^(b) [C II] emission is only detected in the central spaxel.

4. Analysis

4.1. Correlation of line luminosities

In Fig. 5 we investigate the correlation among different line luminosities. We use the Pearson correlation coefficient to quantify the degree of linear correlation². A (linear) correlation is found between the [O I] 145 μ m and [O I] 63 μ m luminosities (panel (a)) with a Pearson coefficient $P = 0.99$. The linear fit gives

$$[\text{O I}]_{145\mu\text{m}} = (0.034 \pm 0.001) \cdot [\text{O I}]_{63\mu\text{m}} + (4.7 \pm 0.26) \cdot 10^{-6} \quad (1)$$

with the line luminosities in units of solar luminosity.

The [C II] (extended emission subtracted, see Sec.3.6) and oxygen line luminosities also appear to be correlated (panel (b) and (c)) with a Pearson coefficient $P = 0.82$ ([C II] - [O I] 63 μ m) and 0.87 ([C II] - [O I] 145 μ m). Given the small number of points, we need to quantify the significance of these coefficients. To do this we perform a significance test (e.g. Taylor 1997). The probability that the [O I] and [C II] lines are not correlated is 2% ([O I] 63 μ m) and 1.3% ([O I] 145 μ m) which implies a confidence limit of 97% and 98% for the [C II] - [O I] 63 μ m and [C II] - [O I] 145 μ m relations, respectively. Note that in the case of HD 38120 the [C II] emission exceeds that of oxygen. If we exclude this object from the analysis the Pearson coefficient is $P = 0.99$ (for both the oxygen lines). The linear fit to the line luminosities gives

² The Pearson coefficient varies between [-1.1], a value close to unity implies a linear correlation between the two variables. A value close to -1 reveals an anti-correlation.

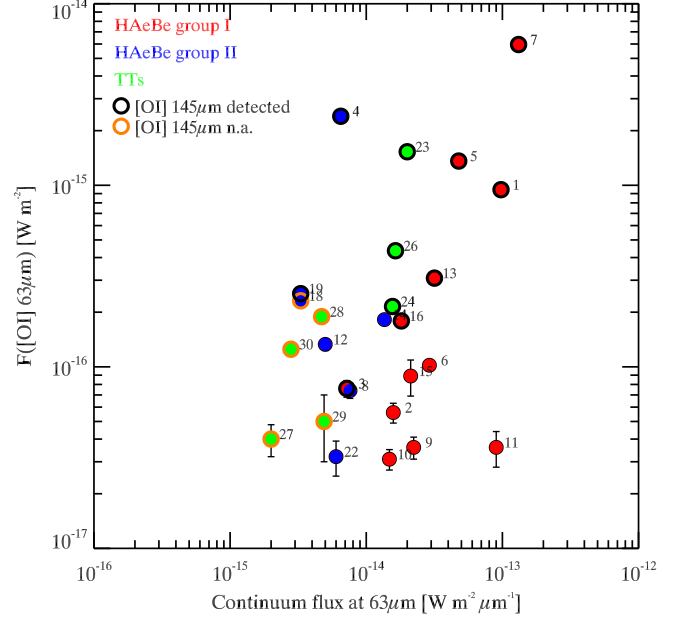


Fig. 6. [O I] 63 μ m line flux versus continuum flux at 63 μ m. Open black circles indicates objects with [O I] 145 μ m detections. Open orange circles indicates object with [O I] 145 μ m data not available. Numbers correspond the the object IDs in Table 1

$$[\text{C II}] = (0.029 \pm 0.001) \cdot [\text{O I}]_{63\mu\text{m}} + (1.27 \pm 0.25) \cdot 10^{-6} \quad (2)$$

$$[\text{C II}] = (0.971 \pm 0.036) \cdot [\text{O I}]_{145\mu\text{m}} - (7.33 \pm 0.52) \cdot 10^{-6} \quad (3)$$

Panel (d) of Fig. 5 shows the line luminosity of the OH ${}^2\Pi_{3/2}J = 9/2 - 7/2$ line at 65 μ m (average of the two lines) versus the [O I] 63 μ m luminosity. The Pearson coefficient is 0.97, suggesting also in this case a linear correlation. The linear fit gives

$$\text{OH}_{65\mu\text{m}} = (0.017 \pm 0.001) \cdot [\text{O I}]_{63\mu\text{m}} + (1.50 \pm 0.04) \cdot 10^{-5} \quad (4)$$

We have also searched for correlations between line and continuum flux. The only finding is that sources with stronger FIR continuum flux can have stronger [O I] 63 μ m line intensity. Nevertheless, the intensity of the [O I] 63 μ m line can vary by more than 2 orders of magnitude for a given value of the continuum luminosity (Fig. 6). No other clear correlations with source parameters are found.

4.2. [C II]-[O I] diagnostic plots

The atomic fine structure lines can be used as diagnostics of the physical conditions of the emitting gas. In this section we analyze the three line ratios: [O I] 145 μ m / [O I] 63 μ m, [O I] 145 μ m / [C II], [O I] 63 μ m / [C II].

With the assumption that the three lines come from the same region the gas density and the incident FUV flux can be estimated by comparing the observations with PDR models. In the high density regime ($> 10^4$ cm⁻³) different PDR models do not converge and may predict very different gas temperatures (e.g. Röllig et al. 2007). Since the oxygen fine structure lines are very sensitive to the temperature, different models produce very different line ratios. The aim of our analysis is to look for a trend

Table 3. OH line fluxes

	² Π _{3/2}				² Π _{1/2} - ² Π _{3/2}			
	9/2 ⁻ - 7/2 ⁺ 65.13 μm	9/2 ⁺ - 7/2 ⁻ 65.28 μm	7/2 ⁻ - 5/2 ⁺ 84.42 μm	7/2 ⁺ - 5/2 ⁻ 84.59 μm	5/2 ⁻ - 3/2 ⁺ 119.23 μm	5/2 ⁺ - 3/2 ⁻ 119.44 μm	1/2 ⁻ - 3/2 ⁺ 79.11 μm	1/2 ⁺ - 3/2 ⁻ 79.18 μm
AB Aur	7.0 ± 2.0	12.5 ± 2.0	10.1 ± 1.5	10.1 ± 1.5	2.8 ± 1.4	3.1 ± 1.4	< 9.0	< 9.0
HD 36112	2.2 ± 0.5	2.9 ± 0.5	2.5 ± 0.8	2.6 ± 0.8	0.49 ± 0.20	0.52 ± 0.12	< 3.4	< 3.4
HD 38120	< 3.5	< 3.5	< 2.8	< 2.8	< 0.9	< 0.9	< 2.7	< 2.7
HD 50138	4.0 ± 0.8	4.1 ± 0.8	^a	1.9 ± 0.6	1.0 ± 0.2	1.1 ± 0.2	< 4.0	< 4.0
HD 97048	4.9 ± 1.0	5.7 ± 1.0	6.8 ± 1.0	6.8 ± 1.0	< 2.4	< 2.4	< 4.0	< 4.0
HD 100453	< 3.4	< 3.4	< 3.0	< 3.0	< 1.3	< 1.3	< 2.0	< 2.0
HD 100546	13.6 ± 0.4	19.9 ± 3.3	^a	13.8 ± 2.0	4.2 ± 0.9	4.2 ± 0.9	< 6.0	< 6.0
HD 104237	3.0 ± 0.5	3.0 ± 0.5	3.1 ± 0.5	3.1 ± 0.5	1.2 ± 0.3	1.2 ± 0.3	< 3.6	< 3.6
HD 135344 B	< 4.0	< 4.0	< 3.8	< 3.8	0.67 ± 0.19	0.71 ± 0.16	< 3.0	< 3.0
HD 139614	< 4.6	< 4.6	< 3.6	< 3.6	< 1.2	< 1.2	< 3.0	< 3.0
HD 142527	< 9.0	< 9.0	6.6 ± 1.1	5.0 ± 2.0	< 4.0	< 4.0	< 4.0	< 4.0
HD 144668	< 4.5	< 4.5	< 4.8	< 4.8	< 0.8	< 0.8	< 4.0	< 4.0
IRS 48	< 9.6	< 9.6	< 4.0	< 4.0	< 1.2	< 1.2	< 3.0	< 3.0
HD 163296	5.3 ± 0.8	4.5 ± 0.8	2.8 ± 0.5	2.7 ± 0.5	1.3 ± 0.2	0.74 ± 0.23	< 3.0	< 3.0
HD 169142	< 8.4	< 8.4	< 7.9	< 7.9	< 2.4	< 2.4	< 4.0	< 4.0
HD 179218	< 3.2	< 3.2	< 2.7	< 2.7	< 1.1	< 1.1	< 2.0	< 2.0
DG Tau	5.9 ± 0.7	8.9 ± 0.7	10.6 ± 0.7	10.4 ± 0.7	2.6 ± 0.4	3.8 ± 0.4	4.7 ± 0.8	4.7 ± 0.8
AS 205	6.5 ± 1.0	6.4 ± 1.0	4.8 ± 0.8	4.7 ± 0.8	0.8 ± 0.3	1.3 ± 0.3	2.2 ± 0.8	2.5 ± 0.8
SR 21	< 3.8	< 3.8	< 3.9	< 3.8	< 1.3	< 1.3	< 3.5	< 3.5
S CrA	5.0 ± 0.6	5.8 ± 0.6	4.5 ± 0.7	5.1 ± 0.7	absorption	absorption	2.9 ± 0.8	< 4.5

	² Π _{1/2}					
	9/2 ⁻ - 7/2 ⁺ 55.89 μm	9/2 ⁺ - 7/2 ⁻ 55.95 μm	7/2 ⁻ - 5/2 ⁺ 71.17 μm	7/2 ⁺ - 5/2 ⁻ 71.21 μm	3/2 ⁺ - 1/2 ⁻ 163.12 μm	3/2 ⁻ - 1/2 ⁺ 163.40 μm
AB Aur	< 22.4	< 22.4	4.5 ± 0.6	4.5 ± 0.6	< 3.3	< 3.3
HD 36112	< 7.6	< 7.6	1.2 ± 0.2	1.2 ± 0.3	< 1.5	< 1.5
HD 38120	< 5.6	< 5.6	< 2.3	< 2.3	< 1.3	< 1.3
HD 50138	< 8.0	< 8.0	2.0 ± 0.4	2.0 ± 0.4	< 1.8	< 1.8
HD 97048	3.0 ± 0.8	2.4 ± 0.8	1.8 ± 0.4	1.8 ± 0.4	< 2.5	< 2.5
HD 100453	< 5.5	< 5.5	< 3.0	< 3.0	< 1.4	< 1.4
HD 100546	< 16.0	< 16.0	8.0 ± 1.4	8.0 ± 1.4	< 3.7	< 3.7
HD 104237	2.4 ± 0.8	2.7 ± 0.8	1.4 ± 0.3	1.4 ± 0.3	< 1.7	< 1.7
HD 135344 B	< 8.2	< 8.2	< 2.7	< 2.7	< 1.6	< 1.6
HD 139614	< 8.5	< 8.5	< 2.9	< 2.9	< 1.6	< 1.6
HD 142527	< 13.0	< 13.0	< 6.3	< 6.3	< 2.8	< 2.8
HD 144668	< 7.8	< 7.8	< 2.9	< 2.9	< 2.3	< 2.3
IRS 48	< 8.3	< 8.3	< 2.9	< 2.9	< 1.6	< 1.7
HD 163296	4.8 ± 1.0	6.0 ± 1.0	< 1.8	2.9 ± 0.3	< 1.4	< 1.4
HD 169142	< 13.5	< 13.5	< 5.8	< 5.8	< 2.8	< 2.8
HD 179218	< 7.0	< 7.0	< 2.2	< 2.2	< 1.0	< 1.0
DG Tau	5.0 ± 1.0	5.0 ± 1.0	4.0 ± 1.0	4.0 ± 1.0	0.9 ± 0.4	1.3 ± 0.4
AS 205	3.8 ± 1.2	5.6 ± 1.2	2.1 ± 0.6	2.1 ± 0.6	< 1.5	< 1.5
SR 21	< 5.8	< 5.8	< 3.2	< 3.2	< 1.5	< 1.5
S CrA	< 6.0	< 6.0	1.6 ± 0.6	1.9 ± 0.6	< 1.6	< 1.6

Notes. Flux units are 10⁻¹⁷ W m⁻².

^(a) Blended with CO *J*=31-30.

consistent with the observations. For this reason, the comparison of the data to a single PDR model is justified. The model used here is from Kaufman et al. (1999). Fig. 7 shows the observed line ratios and the model predictions. According to this model, there is a group of sources (AB Aur, HD 50138, HD 97048, HD 100546, HD 179218) with gas density $n > 10^5$ cm⁻³ and G_0 between $10^3 - 10^6$. These values correspond to surface temperature $T_S \sim 500$ K - a few 10^3 K at radii where most of the emission originates. The density is lower for IRS 48, DG Tau ($\sim 10^4$ cm⁻³) and HD 38120 (a few 10^2 cm⁻³). As noted before, not all the [C II] emission measured with PACS comes from the same region as the oxygen lines, thus the intrinsic (disk) oxygen-carbon line ratio can be higher than what is found here. A higher [O I]/[C II] ratio shifts the results to even higher gas densities. For

this reason the gas densities found in Fig. 7 should be considered as a lower limit to the gas density of the oxygen emitting region.

4.3. OH and H₂O excitation

In this section the rotational diagrams of OH are analyzed. The measured *Herschel*-PACS line fluxes of all sources are fit in a homogeneous way with a uniform slab of gas in local thermal equilibrium (LTE) including the effects of line opacity and line overlap (Fedele et al. 2012). The analysis of OH and H₂O lines in AS 205, S CrA and DG Tau is presented by Salyk et al., Vicente et al. and Carr et al. in prep., respectively, and includes the *Spitzer* data on those sources. Here the OH lines are re-analyzed using just the PACS data for consistency and comparison with the

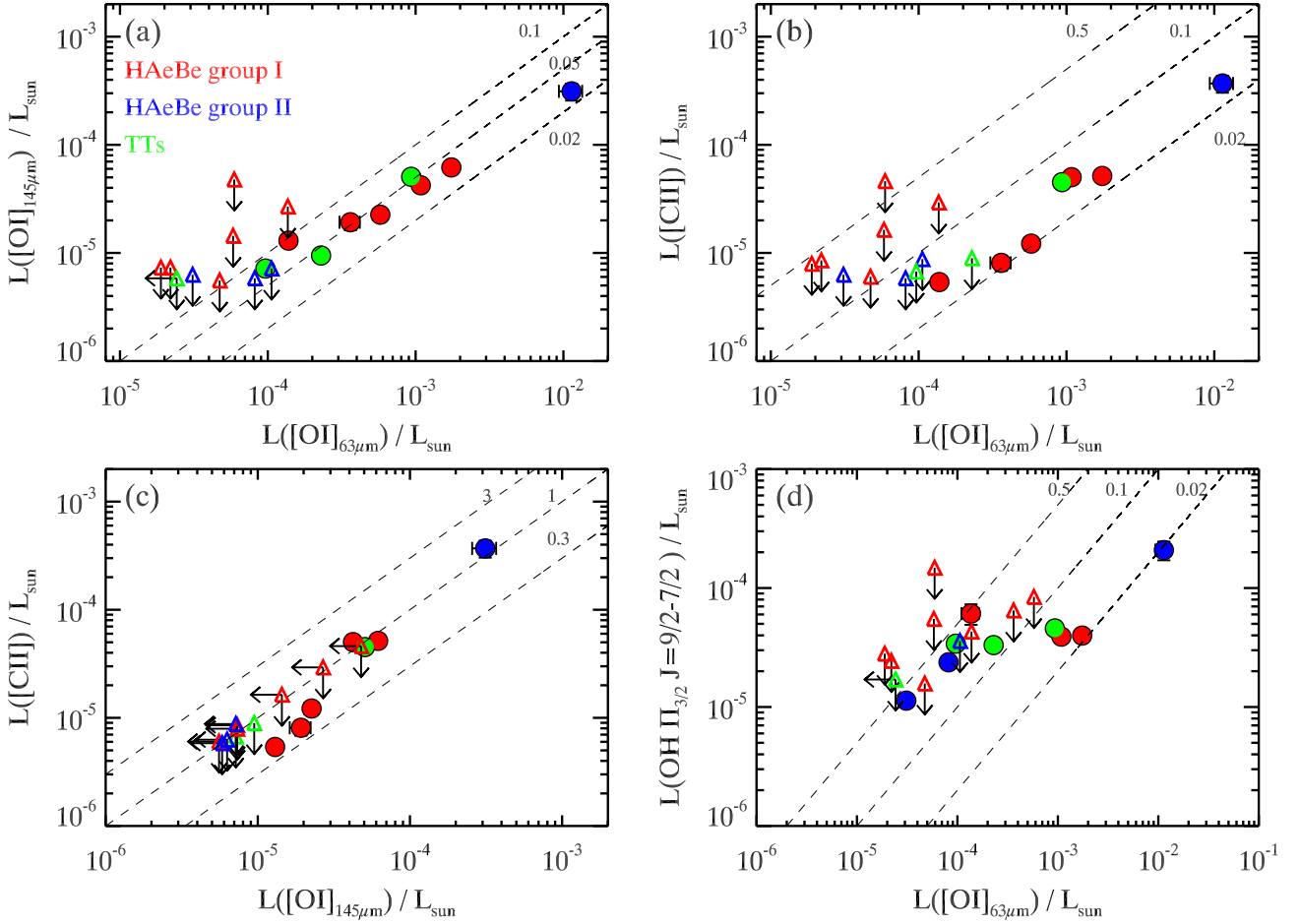


Fig. 5. Correlations between the luminosities of the [O I] and [C II] lines. Dots are the detections, triangles are upper limits.

Herbig AeBe sources, which do not show molecular lines in the *Spitzer* spectra.

4.3.1. Slab model

The molecular emission is assumed to emerge from a disk with homogenous temperature and column density and a radius r . The solid angle is given by $d\Omega_s = \pi r^2 / d^2$, where d is the distance of the source. The flux of an optically thin line can be written as

$$F_{ul} = d\Omega_s \cdot I_{ul} = \pi \frac{r^2}{d^2} \frac{h\nu_{ul}}{4\pi} A_{ul} N_{mol} \frac{g_u e^{-E_u/kT}}{Q(T)} \quad (5)$$

with the line frequency ν_{ul} , the Einstein-A coefficient A_{ul} , the molecular column density N_{mol} , the statistical weight of the upper level g_u , the energy of the upper level E_u and the partition function $Q(T)$. Rearranging eq. 5 yields

$$e^Y \equiv \frac{4\pi F_{ul}}{A_{ul} h\nu_{ul} g_u} = \pi \frac{r^2}{d^2} N_{mol} \frac{e^{-E_u/kT}}{Q(T)} \equiv \pi \frac{r^2}{d^2} \frac{N_u}{g_u} \quad (6)$$

Thus

$$Y = \ln \left(\frac{4\pi F_{ul}}{A_{ul} h\nu_{ul} g_u} \right) = \ln \left(\pi \frac{r^2}{d^2} \frac{N_{mol}}{Q(T)} \right) - \frac{E_u}{kT} \quad (7)$$

The free parameters of the model are the excitation temperature T_{ex} and the column density N_{mol} . The emitting area can be determined uniquely for every given combination of T_{ex} and N_{mol} .

If all lines are optically thin, the column density and emitting area (πr^2) are degenerate. In this case we can measure the total number of molecules and constrain the upper limit of N_{mol} and the lower limit of r . For optically thick lines, the spectrum is calculated on a very fine wavelength grid using

$$I_\nu = d\Omega_s B_\nu(T_{ex})(1 - e^{-\tau_\nu}) \quad (8)$$

with τ_ν obtained from the sum of the

$$\tau_\nu^i = \frac{A_{ul} c^2}{8\pi\nu^2} (N_l \frac{g_u}{g_l} - N_u) \phi_\nu \quad (9)$$

over all fine structure components ($i = 1, 2, \dots$). Here, ϕ_{nu} is the normalized line profile function, which is assumed to be a Gaussian with width corresponding to the thermal line width. No further (e.g. turbulent) line broadening is included. More details are given in Bruderer et al. (2010). The best fit parameters are found by minimizing the χ^2 between model and observations.

4.3.2. OH

OH rotational diagrams have been fitted only for sources for which 4 (or more) OH doublets have been detected. The OH rotational diagrams are presented in Fig. 8-9 where the PACS measurements are shown as red dots and the best-fit model as blue stars. The figure also shows the χ^2 contours of the fit to the data; that of HD 163296 is reported in Fedele et al. (2012). For most

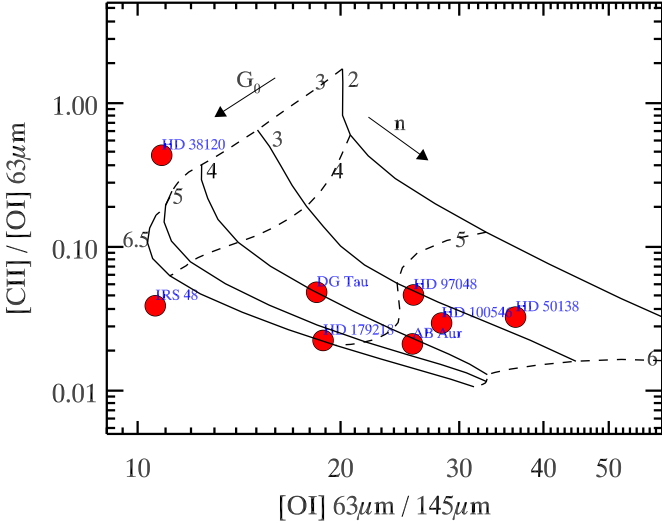


Fig. 7. Observed line ratios of the atomic fine structure lines and PDR model predictions. The continuous lines indicate the region of constant G_0 for values $10^2 - 3.6 \times 10^6$. The dashed lines indicate the iso-density surface for values of $10^2 - 10^6 \text{ cm}^{-3}$.

of the object the OH emission is characterized by a warm temperature with $T_{\text{ex}} \sim 200\text{-}400 \text{ K}$ (AB Aur, HD 97048, HD 100546, HD 36112, HD 163296, AS 205). For some sources all the OH lines are optically thin ($N_{\text{mol}} \lesssim 10^{15} \text{ cm}^{-2}$). For these sources, the OH column density and emitting radius are degenerate so only a lower boundary to the emitting radius is given, varying between 20 and 50 AU. In the case of HD 50138 and DG Tau we find a lower temperature ($T_{\text{ex}} \sim 100\text{-}130 \text{ K}$). Note that low T_{ex} does not necessarily imply a lower kinetic temperature of the gas as it can also be caused by lower density (sub-thermal excitation, e.g. Herczeg et al. 2012).

4.3.3. H₂O

Fig. 10 shows the χ^2 contours for AS 205 (TBC, Salyk et al. in prep.) and RNO 90. Individual analysis of HD 163296 and S CrA is reported respectively in Fedele et al. (2012) and Vicente et al. (in preparation). For the Herbig Ae source HD 163296 Fedele et al. (2012) find that the far-infrared H₂O emission is optically thin, $N_{\text{mol}} \lesssim 10^{15} \text{ cm}^{-2}$ with an emitting radius $r \sim 20 \text{ AU}$ and excitation temperature is $T_{\text{ex}} \sim 200 - 300 \text{ K}$. For the other Herbig sources, HD 142527 and HD 104237, the individual H₂O lines are too weak (below 3σ) for such an analysis. With the assumption of optically thin emission, the number of warm water molecules is

$$N(\text{H}_2\text{O}) = \frac{I(\text{H}_2\text{O}) Q(T) \exp(E_u/kT)}{h \nu_{ul} A_{ul} g_u} \quad (10)$$

with $I(\text{H}_2\text{O})$ the line luminosity, $Q(T)$ partition sum, E_u upper level energy, ν_{ul} transition frequency, A_{ul} Einstein coefficient, g_u upper level degeneracy, k Boltzmann's constant and h Planck's constant. For this calculation we used the upper limit to the $7_{07} - 6_{16}$ line at $72 \mu\text{m}$. The molecular data are from the JPL database and the partition sum is taken from HITRAN TIPS program (Laraia et al. 2011). The typical upper limit to the total number of warm water molecules is from \sim a few $10^{43} - 10^{45}$ for $T = 300 \text{ K}$. This number decreases by $\sim 20\%$ for a gas temperature $T = 400 \text{ K}$. Assuming a characteristic emitting

Table 4. CH⁺ line fluxes ($10^{-17} \text{ W m}^{-2}$)

Transition	Wavelength (μm)	HD 100546	HD 97048
$J = 6 - 5$	60.248	18.5 ± 2.0	2.9 ± 1.5
$J = 5 - 4$	72.141	14.8 ± 2.0	2.2 ± 0.5
$J = 4 - 3$	90.017	13.1 ± 2.0	< 3.0
$J = 3 - 2$	119.858	2.8 ± 2.0	< 2.5
$J = 2 - 1$	179.605	4.2 ± 1.7	< 2.7

Table 5. H₂O line fluxes ($10^{-17} \text{ W m}^{-2}$). TBC whether AS 205 fluxes in this paper.

Transition	Wavelength (μm)	AS 205
$4_{32} - 3_{21}$	58.711	2.5 ± 1.1
$7_{26} - 6_{15}$	59.986	2.4 ± 0.7
$7_{16} - 6_{25}$	66.103	3.0 ± 1.1
$3_{30} - 2_{21}$	66.439	2.9 ± 1.1
$7_{07} - 6_{16}$	71.963	3.1 ± 1.1
$3_{21} - 2_{12}$	75.386	2.0 ± 0.8
$4_{23} - 3_{12}$	78.746	2.7 ± 1.0
$6_{15} - 5_{24}$	78.928	2.8 ± 1.0
$6_{06} - 5_{15}$	83.289	1.7 ± 0.7
RNO 90		
$9_{28} - 9_{19}$	62.434	3.6 ± 1.0
$6_{61} - 6_{52}$	63.910	1.8 ± 0.7
$7_{61} - 7_{52}$	63.939	2.3 ± 0.7
$7_{16} - 6_{25}$	66.095	1.7 ± 0.7
$7_{17} - 6_{06}$	71.551	1.9 ± 0.7
$4_{04} - 3_{13}$	125.359	0.8 ± 0.3
$7_{25} - 7_{16}$	127.869	0.6 ± 0.3
S CrA		
$8_{18} - 7_{07}$	63.310	2.3 ± 0.6
$7_{16} - 6_{25}$	66.087	1.6 ± 0.6
$7_{07} - 6_{16}$	71.966	2.4 ± 0.7
$4_{23} - 3_{12}$	78.768	2.3 ± 0.7
$4_{13} - 4_{04}$	187.110	1.2 ± 0.4

Table 6. Results of the slab model

	T_{ex} [K]	N_{mol} [cm^{-2}]	r [AU]
OH			
AS 205	190	8×10^{15}	19
DG Tau	115	4×10^{15}	50
AB Aur	190	$< 10^{14}$	> 50
HD 36112	240	$< 10^{14}$	> 50
HD 50138	130	2×10^{15}	95
HD 100546	210	2×10^{14}	40
HD 104237	160	2×10^{15}	20
HD 163296	425	8×10^{14}	15
H ₂ O			
AS 205	120	$> 10^{17}$	28
RNO 90	160	$> 10^{17}$	17
HD 163296	250-300	$10^{14} - 10^{15}$	20

radius of 30 AU the upper limit to the water column density, $N_{\text{mol}} = N(\text{H}_2\text{O})/(\pi R^2)$, is a few 10^{14} cm^{-2} (10^{15} cm^{-2} for HD 50138).

In the case of the T Tauri sources AS 205 and RNO 90, the H₂O emission is at the border of optically thick with $T_{\text{ex}} \sim 100 - 300 \text{ K}$ and a column density $N_{\text{mol}} > 10^{16} \text{ cm}^{-2}$. According to the slab model, the emitting radius is $r \sim 15 - 30 \text{ AU}$.

Table 7. H₂O results

$T = 200 \text{ K}$		$T = 300 \text{ K}$	
N	N	N	N
(molecules)	(cm ⁻²)	(molecules)	(cm ⁻²)

5. Discussion

5.1. Origin of far-infrared emission lines

According to the results of the OH rotational diagram, the sample presented here can be divided in two groups: the first group is characterized by optically thin ($N_{\text{mol}} \lesssim 10^{15} \text{ cm}^{-2}$) OH emission with emitting radius $\gtrsim 30 \text{ AU}$. The sources belonging to this group are HD 36112, HD 104327, HD 100546, and AS 205. The derived excitation temperature of the OH emission in Herbig AeBe disks ($T_{\text{ex}} \sim 200 - 400 \text{ K}$) and the emitting radius are consistent with a disk origin with the emission coming from the upper layers of the disk at distances of 20–50 AU from the star. Given the high excitation temperature and high critical densities (of order 10^8 cm^{-3} to excite OH), the emitting radius cannot be much larger. In the case of HD 50138 we found a lower excitation energy ($T_{\text{ex}} \sim 100 \text{ K}$) and a larger emitting radius ($\sim 100 \text{ AU}$). DG Tau also shows “cold” OH emission. The OH emitting radius is $\sim 50 \text{ AU}$, which is 2.5 times larger the emitting radius of the other T Tauri star (AS 205). Given the large emitting area in HD 50138 and DG Tau, it is possible that a further contribution to the OH lines is produced in a shock associated with a molecular outflow in a remnant envelope. Indeed, compact warm OH emission has been observed to be associated outflows in embedded young stellar objects (van Kempen et al. 2010; Wampfler et al. 2010, 2011; Podio et al. 2012, Karska et al. 2012, submitted).

For the two T Tauri stars in which H₂O lines are detected (AS 205 and RNO 90) the derived emitting radius is $\sim 10 - 30 \text{ AU}$, also consistent with a disk origin.

The flux of the oxygen fine structure lines is consistent with a disk origin for most of the sources. The line ratios can be fitted with PDR models and give gas densities $n > 10^5 \text{ cm}^{-3}$ and high UV fluxes. The [C II] emission is spatially extended in all sources where the line is detected. This suggests that there is a contribution from a diffuse cloud (or remnant envelope) around the young star. HIFI spectra of the [C II] line profiles are needed to determine its origin (Fedele et al., in prep.).

5.2. Disk geometry and dust settling

The protoplanetary disks presented here have a different geometry and a different degree of grain growth and settling. These factors are important for the excitation of the atomic and molecular gas. For example, in the case of water, a combination of these factors can play a role in the low detection rate towards Herbig AeBe systems as pointed out by Woitke et al. (2009), whether or not the puffed-up inner rim shadows the hot water layer is important, since shadowing reduces the UV radiation field by about two orders of magnitude and increases water by the same amount. Also, grain settling, presence or absence of PAHs and the gas-to-dust ratio can all have a large effect in boosting line fluxes (e.g., Meijerink et al. 2009; Tilling et al. 2012; Bruderer et al. 2012).

The [O I] 63 μm line is detected in most of the disks independently from disk geometry and stellar parameters. The high detection rate toward group II sources is interesting. If these sources are indeed self-shadowed and/or have grain growth and

settling, the gas temperature in the surface layers should be lower (Jonkheid et al. 2007) and the atomic and molecular emission at far-IR wavelengths is expected to be drastically reduced in group II disks. The excitation of the O (³P₁) level (upper level of the [O I] 63 μm line) is mostly due to collisions with H and H₂. Once the gas density overcomes the critical density of the line ($n_{\text{crit}}([\text{O I}] 63 \mu\text{m}) = 2.5 \cdot 10^5 \text{ cm}^{-3}$ at 100 K) a higher gas temperature is required to further excite the oxygen atoms. In this scenario, group I sources can have stronger [O I] 63 μm and [O I] 145 μm emission due to the higher temperature of the gas. The lower detection rate of [O I] 145 μm emission in group II sources is in line with this hypothesis.

There are differences also among group I sources. The intensity of the [O I] 63 μm line varies by two orders of magnitude for a given value of the continuum flux at 63 μm . This implies a different gas density structure (in the [O I] forming region) from object to object.

According to model predictions (e.g. Woitke et al. 2009; Bruderer et al. 2012), the oxygen emitting region is more extended than the far-infrared continuum. The FIR continuum emission comes mostly from the inner $\sim 50 \text{ AU}$, while the oxygen lines originate in the outer disk (up to a few 10^2 AU in the case of Herbig AeBe stars). The large spread in [O I] 63 μm fluxes for a given FIR continuum flux suggests that the [O I]-bright sources might have an enhanced scale-height (more flared) compared to the [O I]-faint sources. Interestingly only the [O I]-bright sources show [C II] emission.

In paper I we found that far-IR CO emission is only detected in HAeBe systems of group I. The high- J CO lines detected with PACS are sensitive to the UV flux impinging onto the disk, which controls the disk gas temperature. Using the thermochemical models of Bruderer et al. (2012), we showed that flared disks indeed have higher gas temperatures out to several tens of AU and stronger high- J CO fluxes. This is an independent proof that the disks of group I indeed have a flared geometry. On the other hand, the OH lines are less sensitive to the gas temperature, consistent with its detection in both Group I and II sources (Bruderer et al., in prep.).

An alternative scenario is that the total gas mass is different with group I sources having higher disk mass. In this case the oxygen line intensity correlates with the gas mass. We find this solution very unlikely as there is no evidence that group I sources have higher disk masses. No correlation is found between the [O I] 63 μm intensity and the 1.3 mm continuum.

5.3. Comparison to near- and mid-IR spectroscopy

The comparison of the far-infrared spectra shown here to the near- (1–5 μm) and mid- (10–40 μm) IR spectra can give us insights on the radial distribution of different gas species in the upper layers of protoplanetary disks.

Herbig AeBe: The major difference between short and long wavelengths is the lack of any H₂O lines at near-IR (Mandell et al. 2008; Fedele et al. 2011) whereas weak H₂O lines are detected at mid- and far-IR in some sources (Pontoppidan et al. 2011; Fedele et al. 2012; Meeus et al. 2012). Even though the detection rate of warm H₂O is low and the individual lines are weak ($< \text{a few } 10^{17} \text{ W m}^{-2}$), this finding suggests a different H₂O abundance between the inner and outer disk. Also interesting is the high detection rate ($\sim 40\%$) of far-infrared OH emission for sources with full spectral coverage. This emission is detected in both group I and II sources in contrast to near-IR OH emission which is preferentially detected in group I sources only (Fedele

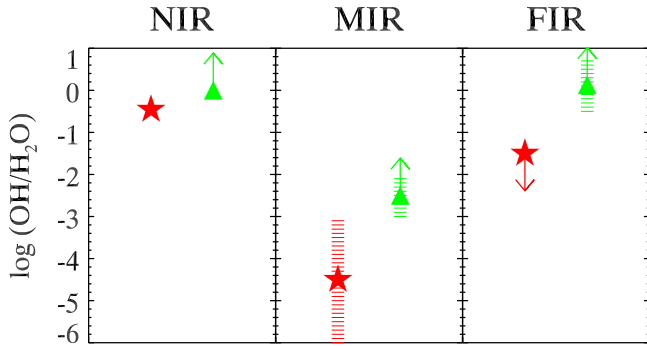


Fig. 11. OH/H₂O ratio for T Tauri (red stars) and Herbig AeBe (green squares). The dashed regions indicate the range of observed ratio.

et al. 2011). In paper I we found that far-infrared CO lines are mainly detected toward group I sources in contrast to near-IR ro-vibrational CO lines which are detected in both groups. It is very unlikely that this is due to a different CO abundance between the two groups in the outer disk. Instead it is likely a consequence of the larger number of UV photons that impinge onto the disk surface in the case of a flared geometry which can heat the gas to the larger distances responsible for the far-IR lines.

T Tauri : the PACS spectra presented here reveal are rich in molecular emission similar to the near-IR and mid-IR spectra. AS 205 and RNO 90 have a rich OH and H₂O spectrum ranging from pure-rotational lines detected here to ro-vibrational lines detected with NIRSPEC and CRIRES (3 μm) and *Spitzer*/IRS (10–40 μm) (Salyk et al. 2011b; Pontoppidan et al. 2011; Mandell et al. 2012). The energy levels involved range from a few hundreds to a few thousands K. The H₂O-rich PACS spectrum is unlikely to originate from the same region of the disk as the shorter wavelength data. Indeed, based on the slab model, the emitting region of the far-IR lines of OH and H₂O has a radius $r \sim 20\text{--}30$ AU in contrast to a radius of a few AU for the hot H₂O near-IR and mid-IR lines (Salyk et al. 2011b). The conclusion is that disks around low-mass pre-main sequence stars are chemically active and H₂O rich from the inner (~ 0.1 AU) to the outer (~ 30 AU) disk.

Fig. 11 shows the OH/H₂O ratio for T Tauri and Herbig AeBe stars measured at different wavelengths. The values represent the ratio of the total number of molecules and are taken from Salyk et al. (2008), Fedele et al. (2011), Salyk et al. (2011a) and from this work. In the case of Herbig AeBe stars, the MIR ratio refers to the ratio of the upper limits. In all wavelength ranges, the Herbig AeBe disks show a lower H₂O abundance compared to T Tauri stars.

5.4. Disk chemistry

The different detection rates and excitation mechanisms of the various species provide information about the chemical processes governing the atmosphere of protoplanetary disks. In the case of the UV-bright Herbig stars, the chemistry and excitation are regulated more strongly by photoprocesses like UV fluorescence (e.g. for CO) and photodissociation of molecules (e.g. OH, H₂O) than in T Tauri stars, unless those low-mass sources have significant UV excess due to accretion.

First, we find that OH far-IR emission is detected in all groups of sources in contrast to CO far-IR emission which is only detected in flared Herbig AeBe disks and T Tauri disks.

The excitation of the high- J CO rotational lines in disks is regulated by the gas temperature which in turn is controlled by the UV radiation field. This is not the case of the OH lines which are excited either by collisions with atomic and molecular hydrogen and through infrared pumping. A third viable mechanism for OH is the prompt emission where the OH molecules are produced rotationally excited by the photodissociation of water. The detection of (weak) H₂O emission and the presence of OH in disks with less UV in the outer region (T Tauri and Herbig AeBe group II) suggests that the prompt emission process does not dominate.

Another interesting finding is the detection of (weak) far-infrared H₂O emission. The non-detection of hot H₂O lines at near- and mid-IR wavelengths suggests that the atmospheres of disks around early type stars are depleted in H₂O molecules due to the photodissociation of H₂O by the strong UV radiation field of the central star (Fedele et al. 2011; Pontoppidan et al. 2011). In contrast, the PACS detection of warm H₂O in some sources suggests that H₂O molecules can survive at large distance (> 30 AU) from the star, likely produced by high temperature reactions of O + H₂ and OH + H₂ driving much of the oxygen into water (e.g., Bergin 2011; Woitke et al. 2010). The importance of this result is that it reveals the presence of an H₂O reservoir in the outer disk around early type stars, beyond the traditional snow line. The formation of OH and H₂O in the H₂-rich warm molecular layer traced by the far-infrared lines is regulated by gas-phase reactions



which requires high gas temperature to occur ($T > 300$ K).

CH⁺ emission is found toward HD 100546 and HD 97048. Interestingly these are the only two Herbig AeBe sources where ro-vibrational H₂ emission has been detected so far (Carmona et al. 2011). The velocity profile of the line suggests extended H₂ emission to more than 50 AU (radius) from the star (Carmona et al. 2011). This is likely the same spatial region traced by the far-IR CH⁺ lines reported here. The detection of vibrationally excited H₂ and CH⁺ towards the same sources is not a coincidence but relates to the gas phase reaction



If H₂^{*} is vibrationally excited, the forward reaction (which is endothermic by ~ 4000 K) is faster (see also Agúndez et al. 2010; Thi et al. 2011).

6. Conclusion

We present far-infrared spectra of Herbig AeBe and T Tauri stars taken with Herschel/PACS. Besides the fine structure lines of [O I] and [C II], emission is detected of CO (paper I), OH, H₂O, CH⁺. The most common feature detected is the [O I] 63 μm line.

Far-infrared OH emission is detected in several sources. A LTE slab model including optical depth effects is used to fit the OH rotational diagram. The OH lines are likely associated with the disk, probing a warm layer of gas in the outer disk ($r \gtrsim 20$ AU). In the case of HD 50138 and DG Tau some of the OH emission is likely associated with an outflow. In contrast to the high- J CO lines, the OH lines are detected in both flat and flared disks (Group I and II) around Herbig AeBe stars. The reason for this is the different excitation mechanisms for the two species.

Warm H₂O emission is detected in three Herbig AeBe sources and in four T Tauri sources. In the Herbig sources, the emission is weak and the detection of warm H₂O is confirmed only by line stacking. This result reveals the presence of a H₂O reservoir in the outer disk region around Herbig stars, in contrast with their H₂O-poor inner region (Mandell et al. 2008; Pontoppidan et al. 2011; Fedele et al. 2011). However, a non-disk origin cannot be excluded based on the PACS lines only. In the case of the T Tauri stars (AS 205 and RNO 90) the slab model suggests “cold” (T_{ex} 100–150 K) H₂O emission coming from a the inner 20–30 AU from the star.

Acknowledgements. We are grateful to the DIGIT team for stimulating discussions and scientific support. Astrochemistry in Leiden is supported by the Netherlands Research School for Astronomy (NOVA), by a Spinoza grant and grant 614.001.008 from the Netherlands Organisation for Scientific Research (NWO), and by the European Community’s Seventh Framework Programme FP7/2007–2013 under grant 238258 (LASSIE) and grant 291141 (CHEMPLAN). PACS has been developed by a consortium of institutes led by MPE (Germany) and including UVIE (Austria); KU Leuven, CSL, IMEC (Belgium); CEA, LAM (France); MPIA (Germany); INAF-IFSI/OAA/OAP/OAT, LENS, SISSA (Italy); IAC (Spain). This development has been supported by the funding agencies BMVIT (Austria), ESA-PRODEX (Belgium), CEA/CNES (France), DLR (Germany), ASI/INAF (Italy), and CICYT/MCYT (Spain).

References

- Acke, B., Min, M., van den Ancker, M. E., et al. 2009, *A&A*, 502, L17
 Agúndez, M., Goicoechea, J. R., Cernicharo, J., Faure, A., & Roueff, E. 2010, *ApJ*, 713, 662
 Bergin, E. A. 2011, *The Chemical Evolution of Protoplanetary Disks*, ed. P. J. V. Garcia, 55–113
 Blake, G. A. & Boogert, A. C. A. 2004, *ApJ*, 606, L73
 Brittain, S. D., Rettig, T. W., Simon, T., et al. 2003, *ApJ*, 588, 535
 Bruderer, S., Benz, A. O., Stäuber, P., & Doty, S. D. 2010, *ApJ*, 720, 1432
 Bruderer, S., van Dishoeck, E. F., Doty, S. D., & Herczeg, G. J. 2012, *A&A*, 541, A91
 Carmona, A., van der Plas, G., van den Ancker, M. E., et al. 2011, *A&A*, 533, A39
 Creech-Eakman, M. J., Chiang, E. I., Joungh, R. M. K., Blake, G. A., & van Dishoeck, E. F. 2002, *A&A*, 385, 546
 Fedele, D., Bruderer, S., van Dishoeck, E. F., et al. 2012, *A&A*, 544, L9
 Fedele, D., Pascucci, I., Brittain, S., et al. 2011, *ApJ*, 732, 106
 Henning, T., Semenov, D., Guilloteau, S., et al. 2010, *ApJ*, 714, 1511
 Herczeg, G. J., Karska, A., Bruderer, S., et al. 2012, *A&A*, 540, A84
 Jonkheid, B., Dullemond, C. P., Hogerheijde, M. R., & van Dishoeck, E. F. 2007, *A&A*, 463, 203
 Juhász, A., Bouwman, J., Henning, T., et al. 2010, *ApJ*, 721, 431
 Kamp, I. & Dullemond, C. P. 2004, *ApJ*, 615, 991
 Kaufman, M. J., Wolfire, M. G., Hollenbach, D. J., & Luhman, M. L. 1999, *ApJ*, 527, 795
 Laraia, A. L., Gamache, R. R., Lamouroux, J., Gordon, I. E., & Rothman, L. S. 2011, *Icarus*, 215, 391
 Lorenzetti, D. 2005, *Space Sci. Rev.*, 119, 181
 Lorenzetti, D., Giannini, T., Nisini, B., et al. 2000, *A&A*, 357, 1035
 Lorenzetti, D., Giannini, T., Nisini, B., et al. 2002, *A&A*, 395, 637
 Mandell, A. M., Bast, J., van Dishoeck, E. F., et al. 2012, *ApJ*, 747, 92
 Mandell, A. M., Mumma, M. J., Blake, G. A., et al. 2008, *ApJ*, 681, L25
 Meeus, G., Montesinos, B., Mendigutía, I., et al. 2012, *A&A*, 544, A78
 Meeus, G., Waters, L. B. F. M., Bouwman, J., et al. 2001, *A&A*, 365, 476
 Meijerink, R., Pontoppidan, K. M., Blake, G. A., Poelman, D. R., & Dullemond, C. P. 2009, *ApJ*, 704, 1471
 Najita, J., Carr, J. S., & Mathieu, R. D. 2003, *ApJ*, 589, 931
 Pascucci, I., Apai, D., Luhman, K., et al. 2009, *ApJ*, 696, 143
 Pilbratt, G. L., Riedinger, J. R., Passvogel, T., et al. 2010, *A&A*, 518, L1
 Podio, L., Kamp, I., Flower, D., et al. 2012, *A&A*, 545, A44
 Poglitsch, A., Waelkens, C., Geis, N., et al. 2010, *A&A*, 518, L2
 Pontoppidan, K. M., Blake, G. A., & Smette, A. 2011, *ApJ*, 733, 84
 Röllig, M., Abel, N. P., Bell, T., et al. 2007, *A&A*, 467, 187
 Salyk, C., Blake, G. A., Boogert, A. C. A., & Brown, J. M. 2011a, *ApJ*, 743, 112
 Salyk, C., Pontoppidan, K. M., Blake, G. A., et al. 2008, *ApJ*, 676, L49
 Salyk, C., Pontoppidan, K. M., Blake, G. A., Najita, J. R., & Carr, J. S. 2011b, *ApJ*, 731, 130
 Sturm, B., Bouwman, J., Henning, T., et al. 2010, *A&A*, 518, L129

- Taylor, J. 1997, *Introduction to Error Analysis, the Study of Uncertainties in Physical Measurements*, 2nd Edition (University Science Books)
 Thi, W.-F., Ménard, F., Meeus, G., et al. 2011, *A&A*, 530, L2
 Tilling, I., Woitke, P., Meeus, G., et al. 2012, *A&A*, 538, A20
 van der Plas, G., van den Ancker, M. E., Acke, B., et al. 2009, *A&A*, 500, 1137
 van Dishoeck, E. F. 2004, *ARA&A*, 42, 119
 van Kempen, T. A., Kristensen, L. E., Herczeg, G. J., et al. 2010, *A&A*, 518, L121
 Waelkens, C., Waters, L. B. F. M., de Graauw, M. S., et al. 1996, *A&A*, 315, L245
 Wampfler, S. F., Bruderer, S., Kristensen, L. E., et al. 2011, *A&A*, 531, L16
 Wampfler, S. F., Herczeg, G. J., Bruderer, S., et al. 2010, *A&A*, 521, L36
 Woitke, P., Kamp, I., & Thi, W. 2009, *A&A*, 501, 383
 Woitke, P., Pinte, C., Tilling, I., et al. 2010, *MNRAS*, 405, L26

Appendix A: [O I], [C II] spatial extent

This section describes an analysis of the atomic lines aiming at addressing the spatial extent of the line. The Herschel/PACS PSF varies substantially from $50\ \mu\text{m}$ to $200\ \mu\text{m}$. As a consequence the amount of flux in the central spaxel varies from $\sim 70\%$ at $60\ \mu\text{m}$ to 55% at $160\ \mu\text{m}$. For this reason, line emission can be detected outside the central spaxel (especially in the red part $> 100\ \mu\text{m}$). To check whether a line is spatially extended or not we compute the integrated line flux (F_l) and integrated continuum (F_c) next to the line and check the relative spatial distribution.

A.1. [C II] 158 μm

For the [C II] line we integrate the line flux between $157.530 - 157.970\ \mu\text{m}$ and the continuum flux between $158.5 - 162\ \mu\text{m}$. If the line emission is co-spatial to the continuum emission than spatial distribution of the integrated line flux (F_l) will be equal to that of the integrated continuum (F_c) (same PSF). In particular, the distribution of F_c corresponds to the PSF at the given wavelength (assuming that the continuum emission is not spatially resolved). To check the relative distribution of line and continuum we compare the relative integrated flux, that is the flux measured in each spaxel relative to the total flux (measured in the whole PACS array). Fig. A.1 shows the line spectral map for different sources. The spectral map shows the spectrum (continuum subtracted) in each spaxel. X- and Y-range are all the same and scaled to the central spaxel. The numbers represent relative continuum (R_c , black) and line (R_l , red) fluxes. If line and continuum emission are co-spatial, these two numbers must be similar in all spaxels. The maps show instead two main differences: 1) $R_l < R_c$ in the central spaxel; 2) $R_l > R_c$ in some outer spaxels. The most clear cases are HD 38120, IRS 48 and DG Tau. This pattern is the result of extended line emission. In the case of AB Aur and HD 97048 the object is mis-pointed and the spatial distribution of the continuum emission deviates from the PSF. Nevertheless, also in these two cases the difference between R_l and R_c suggests a spatially extended line emission. The case of HD 50138 is less clear.

In the case of the oxygen lines, the emission appears spatially unresolved and co-spatial with the continuum.

A.2. On-source [C II] line flux

To estimate the [C II] emission associated with the protoplanetary disk we need to subtract the extended emission. To do this the [C II] line flux (integrated between $157.60-157.98\ \mu\text{m}$) in each of the 9 central spaxels is calculated. Then the extended emission is determined as the average of the line flux measured in the 8 neighbouring spaxels (around the central one) and subtracted from the value measured in the central spaxel. The result is reported in Table 2. In this way, the large scale ($> 9''.4$) [C II] emission is approximately removed. The value of the [C II] flux derived by this method must be considered an upper limit to the [C II] emission arising from the disk as extended emission from a compact remnant envelope may still be present in the central $9''.4 \times 9''.4$ area of the sky.

Appendix B: Molecular data of selected species

Table B.1. Far-IR OH transitions

Species	Transition	λ [μm]	E_u [K]	$\log(A_{ul})$ [s ⁻¹]
OH	${}^2\Pi_{1/2} 9/2^+ - 7/2^-$	55.891	875	0.34
OH	${}^2\Pi_{1/2} 9/2^- - 7/2^+$	55.949	875	0.34
OH	${}^2\Pi_{3/2} 9/2^- - 7/2^+$	65.131	512	0.11
OH	${}^2\Pi_{3/2} 9/2^+ - 7/2^-$	65.278	510	0.10
OH	${}^2\Pi_{1/2} 7/2^- - 5/2^+$	71.170	617	0.01
OH	${}^2\Pi_{1/2} 7/2^+ - 5/2^-$	71.215	617	0.01
OH	${}^2\Pi_{1/2} - {}^2\Pi_{3/2} J = 1/2^- - 3/2^+$	79.115	181	-1.44
OH	${}^2\Pi_{1/2} - {}^2\Pi_{3/2} J = 1/2^+ - 3/2^-$	79.178	181	-1.44
OH	${}^2\Pi_{3/2} 7/2^- - 5/2^+$	84.420	291	-0.28
OH	${}^2\Pi_{3/2} 7/2^+ - 5/2^-$	84.596	290	-0.28
OH	${}^2\Pi_{3/2} 5/2^- - 3/2^+$	119.233	120	-0.86
OH	${}^2\Pi_{3/2} 5/2^+ - 3/2^-$	119.441	120	-0.86
OH	${}^2\Pi_{1/2} 3/2^+ - 1/2^-$	163.120	270	-1.190
OH	${}^2\Pi_{1/2} 3/2^- - 1/2^+$	163.410	270	-1.190
CH ⁺	$J = 6 - 5$	60.248	839	0.27
CH ⁺	$J = 5 - 4$	72.141	600	0.03
CH ⁺	$J = 4 - 3$	90.017	400	-0.26
CH ⁺	$J = 3 - 2$	119.858	240	-0.66
CH ⁺	$J = 2 - 1$	179.605	120	-1.21
p-H ₂ O	$4_{31} - 3_{22}$	56.31	552	0.16
o-H ₂ O	$9_{09} - 8_{18}$	56.82	1323	0.39
o-H ₂ O	$8_{18} - 7_{07}$	63.32	1070	0.24
o-H ₂ O	$3_{30} - 2_{21}$	66.44	410	0.09
o-H ₂ O	$7_{07} - 6_{16}$	71.95	843	0.06
o-H ₂ O	$3_{21} - 2_{12}$	75.38	305	-0.48
o-H ₂ O	$4_{23} - 3_{12}$	78.74	432	-0.32
o-H ₂ O	$6_{16} - 5_{05}$	82.03	643	0.06
p-H ₂ O	$3_{22} - 2_{11}$	89.98	296	-0.45
o-H ₂ O	$2_{21} - 1_{10}$	108.07	194	-0.59
o-H ₂ O	$4_{14} - 3_{03}$	113.54	323	-0.61
[O I]	${}^3P_1 - {}^3P_2$	63.185	228	-4.05
[O I]	${}^3P_0 - {}^3P_2$	145.535	327	-4.75
[C II]	${}^2P_{3/2} - {}^2P_{1/2}$	157.680	91	-5.64

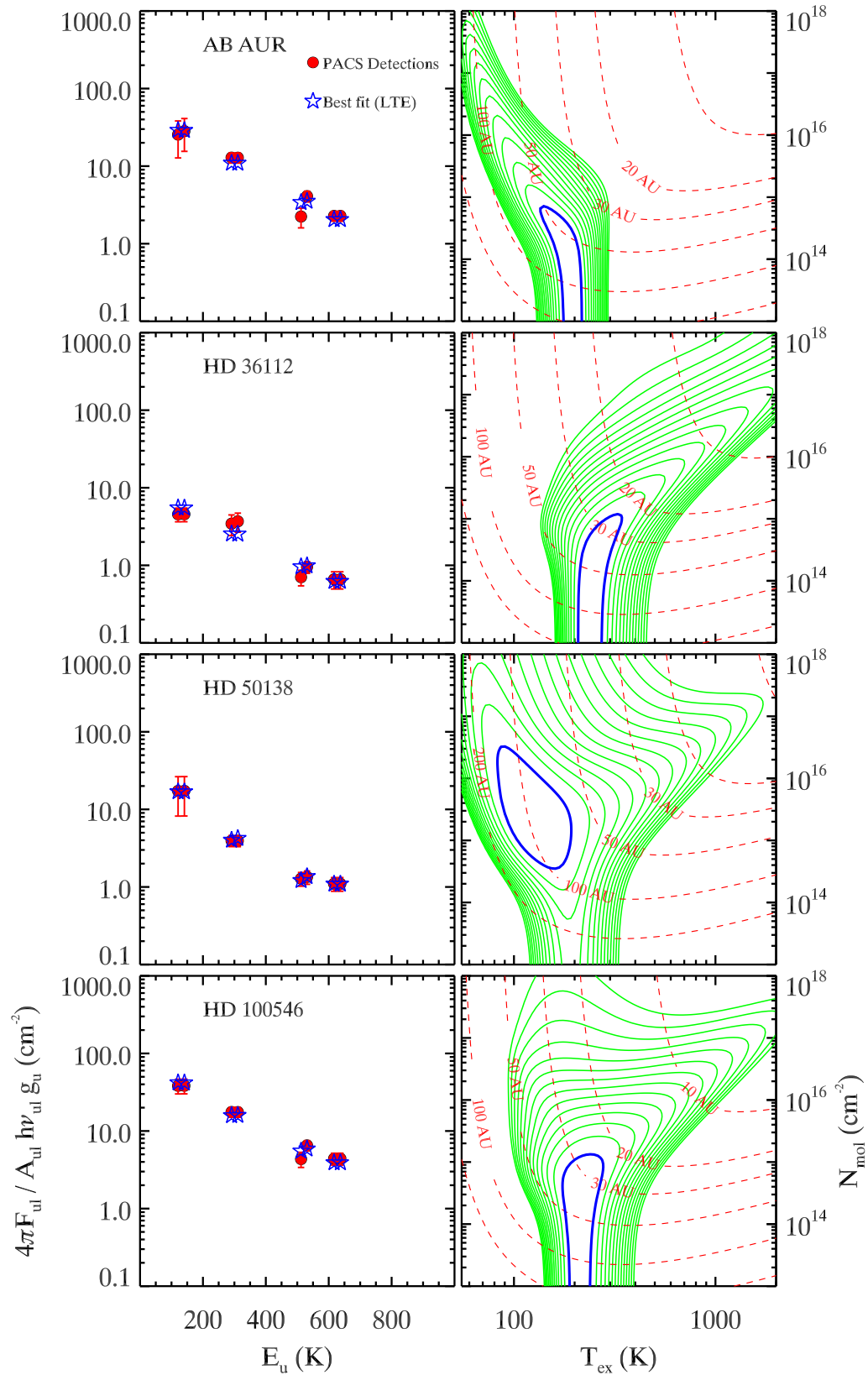


Fig. 8. (left) OH rotational diagram. PACS detections are plotted as (red) dots, best-fit model is shown as (blue) stars. (right) χ^2 contours. The $1-\sigma$ confidence level is highlighted by a (blue) thick line. The (red) dashed lines represent the emitting radius. The blue contour corresponds to the minimum $\chi^2 + 0.5$. The green lines are the χ^2 contours in step of $0.5\chi^2$.

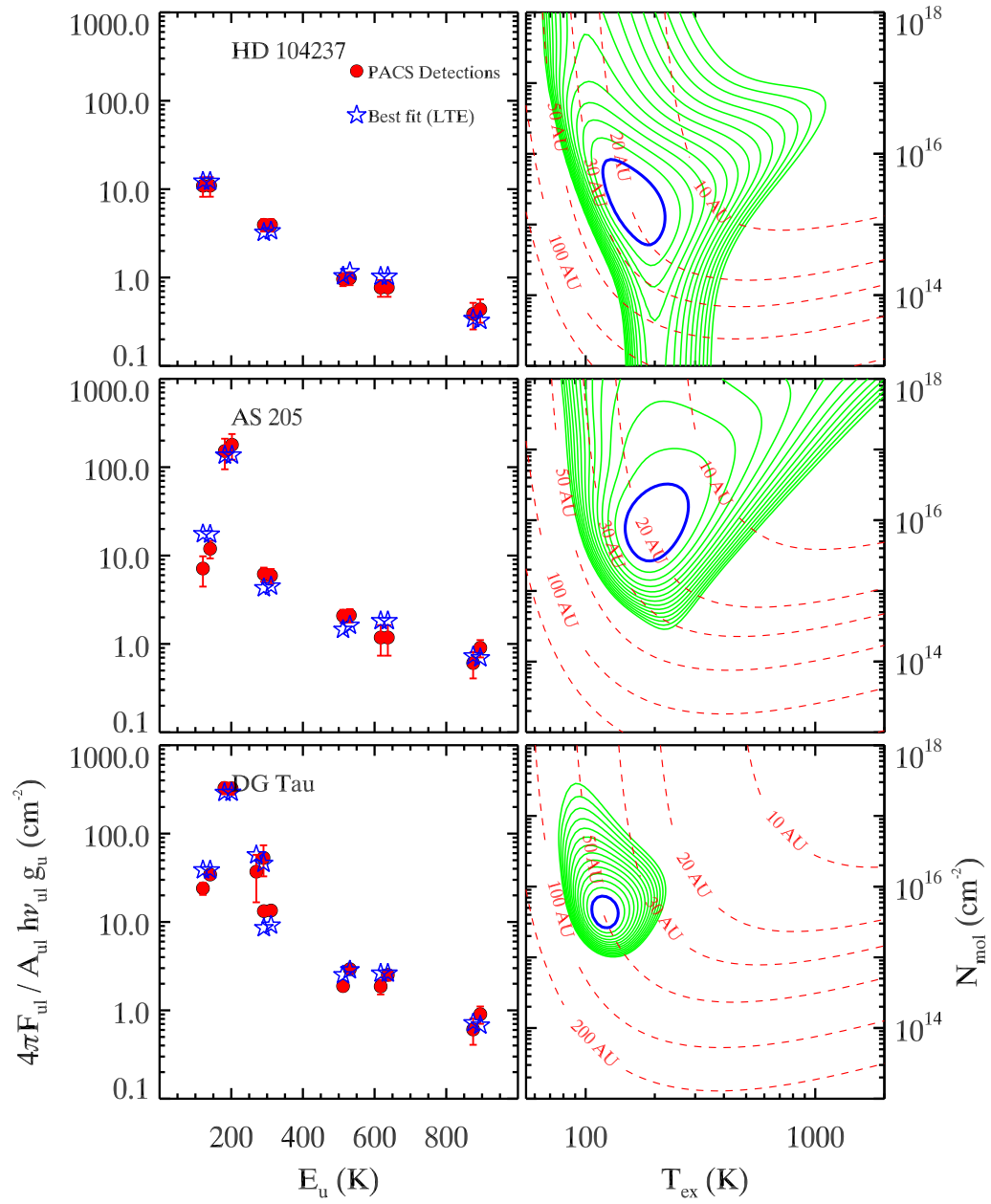


Fig. 9. Continuation of Fig. 8

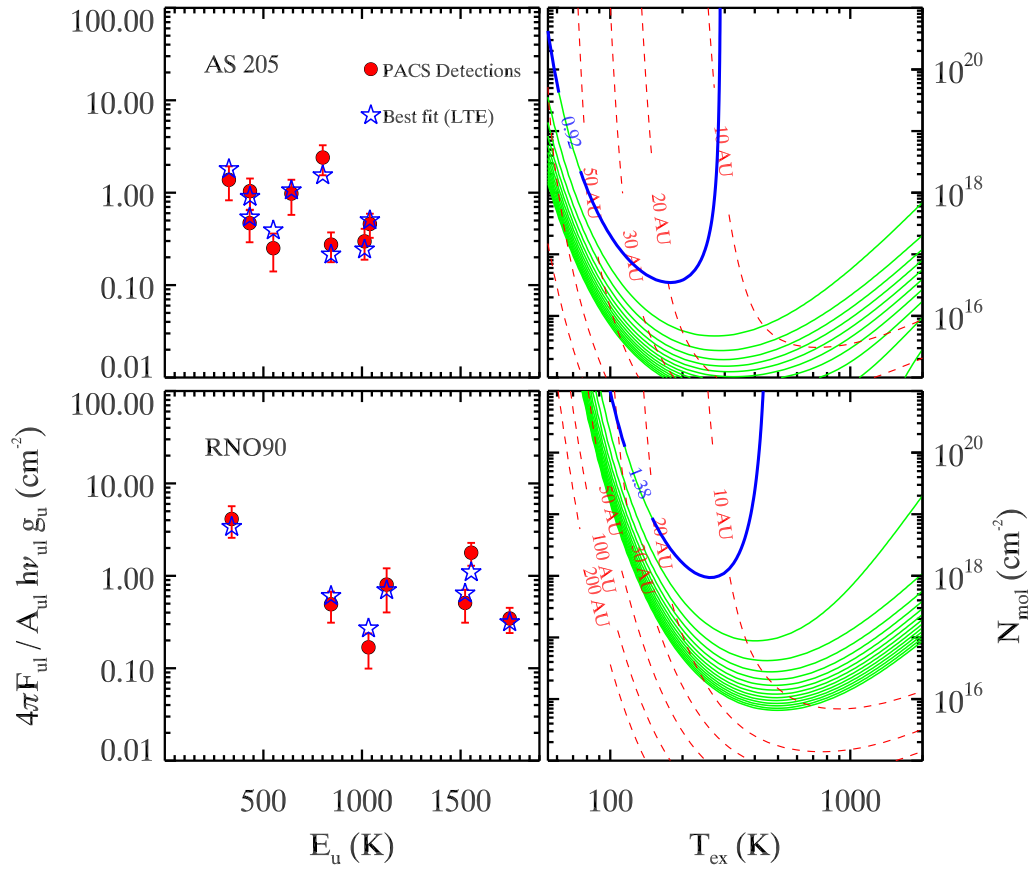


Fig. 10. H₂O rotational diagram (left) and χ^2 contours (right) for AS 205 (top) and RNO 90 (bottom). Colours and symbols as in Figs. 8. *TBC whether AS 205 figure remains in paper.*

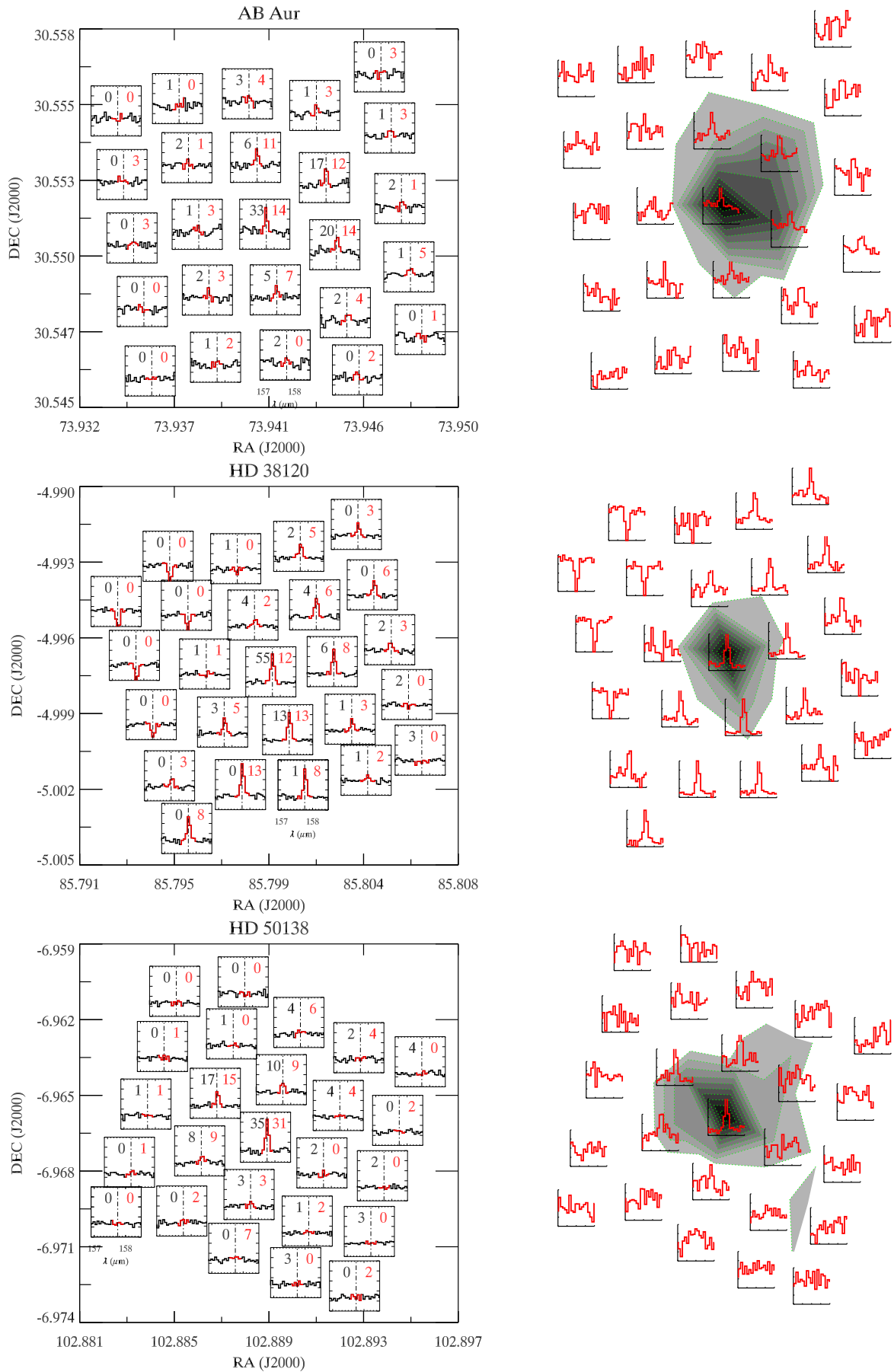


Fig. A.1. [CII] spectral maps. *left:* Each sub-panel shows the continuum-subtracted spectrum. Y-axis is the same in all sub-panels and it is fixed to the Y-axis of the central spaxel. The numbers represent the continuum (black) and line (red) flux relative to the total flux. *right:* The contours represent the continuum distribution measured between 159-163 μm . The last contour level corresponds to 10% of the continuum peak. The sub-panels show the [C II] spectrum. In this case the Y-range is not scaled to the central spaxel.

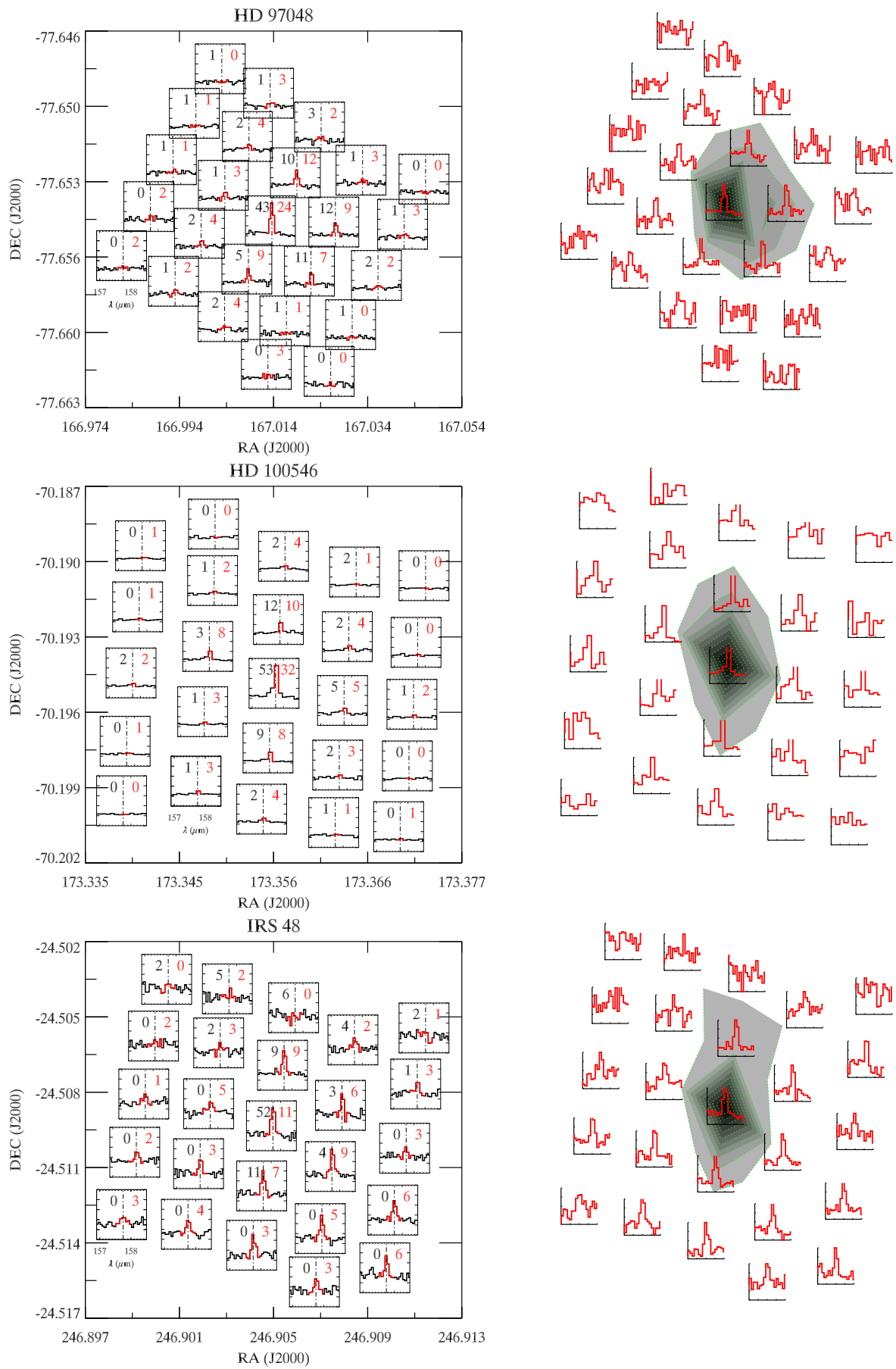


Fig. A.2. Same as Fig. A.1

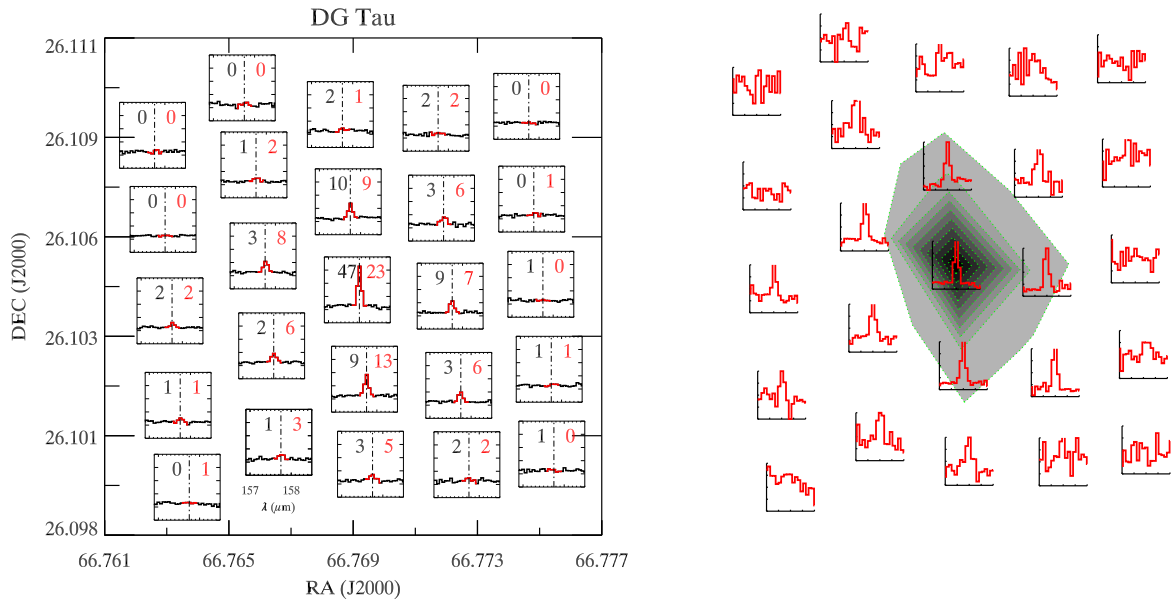


Fig. A.3. Same as Fig. A.1